

1 **Process-based evaluation of ENSO simulation sensitivity to**
2 **horizontal resolution in the Chinese Academy of Sciences FGOALS-**
3 **f3 Climate System Model**

4

5 Meng-Er Song¹, Lin Chen¹, Yongqiang Yu², Bo An², Jiuwei Zhao¹, Hai Zhi¹

6

7 ¹ State Key Laboratory of Climate System Prediction and Risk Management/Key Laboratory of
8 Meteorological Disaster, Ministry of Education/Collaborative Innovation Center on Forecast and
9 Evaluation of Meteorological Disasters, Nanjing University of Information Science and Technology,
10 Nanjing 210044

11 ² State Key Laboratory of Earth System Numerical Modeling and Application, Institute of Atmospheric
12 Physics, Chinese Academy of Sciences, Beijing, China

13

14

15

16 *Correspondence to:* Lin Chen (chenlin@nuist.edu.cn)

17

18

19 **Abstract.** El Niño-Southern Oscillation (ENSO) is the most prominent mode of interannual climate
20 variability, ~~hence~~ its simulation performance thus represents a critical benchmark for evaluating the
21 fidelity of coupled climate models. Increasing model resolution is an effective approach to improve the
22 climate model performancesimulation; however, the impact of refining horizontal resolution from the
23 hundred-kilometer scale to the tens-of-kilometer scale on ENSO simulation, as well as the underlying
24 mechanisms, remains unclear. This study provides a process-based evaluation of ENSO behavior in two
25 versions of the Chinese Academy of Sciences Flexible Global Ocean–Atmosphere–Land System Finite-
26 Volume version 3 (FGOALS-f3) climate system model: a low-resolution configuration (~100 km;
27 FGOALS-f3-L, hereafter f3-L) and a high-resolution configuration (~25 km; FGOALS-f3-H, hereafter
28 f3-H). Using a reproducible diagnostic framework, we assess how horizontal resolution influences ENSO
29 amplitude, oscillation ~~characteristics~~irregularity, key air–sea coupling processes, and high-frequency
30 (HF) atmospheric variability. The low-resolution version severely overestimates ENSO amplitude,
31 whereas f3-H produces amplitude closer to the observation. Process-based diagnostics show that this
32 improvement arises from the more realistic representation of thermocline and zonal advection feedback
33 processes in f3-H, which arises from the more realistic representation of the meridional structure of
34 ENSO-related zonal wind stress anomalies over equatorial Pacific in f3-H and can be traced back to its
35 improved horizontal resolution. The ENSO cycle in f3-L exhibits excessive regularity, featuring periodic
36 warm-cold transitions; while f3-H reproduces an irregular oscillation resembling the observation. The
37 excessive regularity in f3-L is attributed to its coarser resolution, which limits the simulation performance
38 of tropical cyclones and consequently weakens high-frequency westerly wind activity over the tropical
39 Pacific. The ~~feeble~~weak stochastic forcing in f3-L is insufficient to disrupt its overly intense ENSO cycle,
40 yielding an overly regular oscillation. By identifying the structural sources of ENSO biases across
41 resolutions, this study provides a reproducible and model-agnostic framework for diagnosing resolution
42 effects on ENSO performance in climate models and informs future development of the FGOALS-f3
43 model family.

44

45 **1 Introduction**

46 El Niño-Southern Oscillation (ENSO), as one of the most prominent interannual variabilities in the
47 Earth's climate system, exerts a profound influence on regional and global climate (McPhaden et al.,
48 2006; Cai et al., 2021). Therefore, the ability to accurately simulate ENSO phenomenon serves as a
49 fundamental benchmark for evaluating the fidelity of coupled climate models (Timmermann et al., 2018).
50 Despite significant progress in the development of climate models, large inter-model spread remains in
51 ENSO characteristics across Coupled Model Intercomparison Project (CMIP) generations (Zhang et al.,
52 2020; Planton et al., 2021). Common biases include inaccuracies in simulating ENSO amplitude (Planton
53 et al., 2021), period (Lu et al., 2018), seasonal phase locking (Liao et al., 2023; Yan and Sun, 2024),
54 spatial distribution (Jiang et al., 2021), and intensity asymmetry (Zhao and Sun, 2022), as well as [an](#)
55 overly regular ENSO oscillation (Chen et al., 2016a; Guilyardi et al., 2020). These deficiencies reflect
56 systematic structural biases within models, which directly limit the predictive skill of dynamical models
57 (Barnston et al., 2012) and hinder the reliability of climate projection regarding how ENSO may evolve
58 under future climate change (Jiang et al., 2020a). Therefore, it is imperative to improve the fidelity of
59 ENSO simulation in climate models.

60 Horizontal resolution has long been recognized as an important factor influencing model behavior
61 (Yu et al., 2024). Motivated by this, the latest CMIP6 launched a dedicated High-Resolution Model Inter-
62 comparison Project (HighResMIP) (Eyring et al., 2016) to systematically assess the benefits of increased
63 resolution on model simulations. Previous studies have shown that as model resolution increases,
64 simulation capabilities for both the climate mean state and variability exhibit improvements (Dawson et
65 al., 2013; Chang et al., 2020). For example, high-resolution models demonstrate superior performance
66 over low-resolution counterparts in simulating the Asian summer monsoon (He et al., 2025a), the impact
67 of Tibetan Plateau thermal forcing on Asian summer monsoon (He et al., 2025b), the precipitation in
68 southern China (Zi et al., 2024), the spatial distribution and frequency of tropical cyclones (Kreussler et
69 al., 2021; Li et al., 2021), air-sea turbulent flux (Small et al., 2019), heat transport by boundary currents
70 (Docquier et al., 2019), ocean mesoscale eddies (Hallberg, 2013), and Antarctic sea ice (Docquier et al.,
71 2019). This is partly because higher resolution allows models to explicitly resolve finer-scale physical
72 processes, reducing their dependence on parameterization schemes. Furthermore, high-resolution models
73 facilitate a more accurate simulation of topographically sensitive regions, therefore improving the

74 simulation of atmosphere-ocean processes related to complex terrain (Bacmeister et al., 2014; Hewitt et
75 al., 2016). Then a pertinent inquiry arises: does the ENSO simulation benefit from the increased
76 resolution?

77 Regarding the impact of increased horizontal resolution on ENSO characteristics, previous studies
78 found that when the atmospheric horizontal resolution in climate models was increased from 3.8° (T30)
79 or 2.8° (T42) to 1° (T106), significant improvements can be found in the simulated ENSO period
80 (Guilyardi et al., 2004; Navarra et al., 2008) and ENSO amplitude (Hua et al., 2018). However, the
81 aforementioned studies were primarily based on the comparisons from ~400 km (or 300 km) to 100 km
82 scales. In the latest climate models participated in the HighResMIP, model resolutions have advanced
83 substantially, with some achieving 25 km resolution in atmospheric component and 10 km in oceanic
84 component. This higher resolution enables a more realistic reproduction of climate variability, such as
85 tropical cyclones (TCs) (Li et al., 2021) and tropical instability waves (Li et al., 2023). Yet, a critical
86 question remains unresolved: when model resolution reaches ~25 km, a scale that can reasonably
87 simulate weather-scale systems like TCs, does ENSO simulation also improve further?

88 ENSO is fundamentally driven by a number of coupled ocean-atmosphere feedbacks (Li, 1997; Jin
89 et al., 2006; Chen et al., 2015b; Chen et al., 2016a); however, some analyses regarding ENSO simulations
90 are often result-oriented, focusing only on changes in statistical indices while lacking sufficient
91 diagnostic analysis of the key air-sea feedback processes that shape ENSO's properties. Therefore, it is
92 necessary to conduct a process-oriented evaluation when comparing the ENSO simulation between
93 different resolution versions.

94 It is worth noting that the observational evidences have suggested the significant influence of
95 atmospheric "noise" on the development and evolution of ENSO (Chen et al., 2015a; Fedorov et al.,
96 2015). Here the atmospheric "noise" primarily refers to high-frequency (HF) wind activities such as
97 westerly wind bursts (Harrison and Vecchi, 1997; Fedorov, 2002), including synoptic and intra-seasonal
98 scales. TC and Madden-Julian Oscillation (MJO; Madden and Julian, 1971; Madden and Julian, 1972)
99 have been recognized as key sources of HF wind activities in recent studies (Ying et al., 2019; Liang and
100 Fedorov, 2021). Considering the atmospheric components in HighResMIP models can reach a horizontal
101 resolution of 50 km or finer (which is sufficient to reasonably reproduce TC features) and that the
102 simulation performance for TC and MJO activities improves with increasing resolution (Davis, 2018;

103 Tang et al., 2022; Roberts et al., 2025), a further question arises: does the improved simulation of HF
104 activities like TCs and MJO in high-resolution models contribute to improved ENSO simulation?

105 Motivated by these open questions, this study will conduct a process-oriented evaluation of ENSO
106 simulation for a Chinese climate model, the Flexible Global Ocean–Atmosphere–Land System Finite-
107 Volume version 3 (FGOALS-f3) climate system model that was developed by the Institute of
108 Atmospheric Physics, Chinese Academy of Sciences (IAP-CAS). FGOALS-f3 participated in
109 HighResMIP with both a low-resolution (~100 km; FGOALS-f3-L, hereafter f3-L) and a high-resolution
110 version (~25 km; FGOALS-f3-H, hereafter f3-H) (An et al., 2022; Bao et al., 2020). The high-resolution
111 version (f3-H) has been shown to have superior simulation performances over the low-resolution
112 counterpart (f3-L) in representing mesoscale vortices (An et al., 2022), tropical instability waves (Li et
113 al., 2023), TCs (Li et al., 2021), East Asian summer monsoon precipitation (Zi et al., 2024), and the
114 climatological mean states (Yu et al., 2024). Therefore, this study employs the CAS-developed f3-H and
115 f3-L to reveal the impact of model resolution on ENSO simulation performance and the underlying air-
116 sea coupling processes.

117 This model evaluation study will provide insights into the resolution sensitivity of ENSO-related
118 processes in FGOALS-f3 and establishes a diagnostic framework that can be applied to other coupled
119 models participating in CMIP6 and future CMIP phases. The remainder of this paper is organized as
120 follows. Section 2 describes the model configurations, observational datasets, and diagnostic framework.
121 Section 3 presents an overview of the ENSO characteristics in two versions of FGOALS-f3 model.
122 Section 4 and Section 5 demonstrate how the model horizontal resolution impacts the ENSO simulation.
123 Section 6 summarizes the findings and discusses implications for model development and evaluation.

124 **2. Model configurations, datasets, and diagnostic framework**

125 **2.1 Model configurations**

126 FGOALS-f3 is a fully coupled climate system model developed by State Key Laboratory of
127 Numerical Modeling for Atmospheric Sciences and Geophysical Fluid Dynamics (LASG), IAP-CAS,
128 which couples four component models using the CPL7 coupler (Craig et al., 2012). The four component
129 models are the atmospheric model FAMIL2.2 (He et al., 2019; Li et al., 2021), the ocean model
130 LICOM3.0 (Li et al., 2020), the land model CLM4.0 (Lawrence et al., 2011), and the sea ice model

131 CICE4.0 (Hunke and Lipscomb, 2010).

132 The atmospheric component FAMIL2.2 is the last version of the Finite-volume Atmospheric Model
133 developed by the LASG-IAP (FAMIL) (Li et al., 2021). FAMIL2.2 utilizes a finite-volume dynamical
134 core constructed on a cubed sphere grid that is globally partitioned into six tiles (Zhou et al., 2015). In
135 the vertical direction, the model uses hybrid coordinates over 32 layers, and the model top is 1 hPa. While
136 the horizontal resolution ranges from C96 (about 100 km) to C384 (about 25 km) across the different
137 resolution version. The oceanic component LICOM 3.0 is the third version of LASG-IAP Climate System
138 Ocean Model (LICOM) (Yu et al., 2018). LICOM 3.0 updated a new advection scheme and employed a
139 tripolar grid based on orthogonal curvilinear coordinates. The horizontal resolution of LICOM 3.0 can
140 vary flexibly between 1° and $1/20^\circ$. Sub-grid parametrization schemes employed in LICOM 3.0 include
141 the tidal mixing scheme, a buoyancy frequency related thickness diffusivity scheme, a vertical viscosity
142 and diffusion scheme, and a chlorophyll-a dependent solar penetration scheme, etc. A comprehensive
143 description of the physical package in LICOM3.0 can be found in Li et al. (2020). The land component
144 in FGOALS-f3 model is Community Land Model (CLM) version 4.0. This advanced model simulates
145 the water and momentum balances at the land surface and incorporates interactive carbon and nitrogen
146 cycles, allowing for a more realistic representation of vegetation dynamics and ecosystem processes
147 (Lawrence et al., 2011). In FGOALS-f3 model, sea ice is simulated using the Los Alamos Sea Ice Model
148 version 4.0 (CICE 4.0). This is a dynamic-thermodynamic model that simulates the evolution of sea ice
149 thickness, concentration, and velocity. It features multiple ice thickness categories and an elastic-viscous-
150 plastic (EVP) rheology to model ice deformation and dynamics (Hunke and Lipscomb, 2010).

151 The FGOALS-f3 model includes two versions: f3-L and f3-H (He et al., 2019; An et al., 2022). Both
152 models are participating in HighResMIP of CMIP6 and have successfully completed the Tier-1 and Tier-
153 3 experiments. These two models have the same components and physical processes. The sole distinction
154 between f3-H and f3-L lies in their horizontal resolution and the corresponding time steps within their
155 finite-volume cubed-sphere dynamical core (FV3). To maintain the stability of the integration for the
156 dynamical core, the two parameters (k_split and n_split) in FV3 are set to 6 and 15 in f3-H, respectively
157 (they are 2 and 6, respectively, in f3-L). The specific resolutions of each component of f3-L and f3-H
158 models are shown in Table 1.

159

160 **Table 1.** Resolution comparison of each component model between the FGOALS-f3-L model and the FGOALS-f3-
 161 H model

	FGOALS-f3-L	FGOALS-f3-H
Atmosphere	FAMIL2.2 (1°×1°, 32 levels)	FAMIL2.2 (0.25°×0.25°, 32 levels)
Ocean	LICOM3.0 (1°×1°, 30 levels)	LICOM3.0 (0.1°×0.1°, 55 levels)
Land	CLM4.0 (1.25°×0.9°)	CLM4.0 (0.31°×0.23°)
Sea Ice	CICE4.0 (1°×1°)	CICE4.0 (0.1°×0.1°)

162 The model data used in this study are obtained from the historical experiment outputs of f3-L and
 163 f3-H model. Considering the experiment outputs of f3-H (highresSST-present) start from 1950, the period
 164 during 1950-2014 for the two models are analyzed. The main variables used in this study include monthly
 165 sea surface temperature (SST), three-dimensional ocean currents (uo, vo, wo), oceanic potential
 166 temperature (thetao), surface wind stress (tauu, tauv), and net radiation flux (rsds, rsus, rlds, rlus, hfss,
 167 hfls); daily surface wind (uas, vas), precipitation (pr), six-hourly sea level pressure (SLP), 850 hPa wind
 168 (ua, va), 300 hPa and 500 hPa temperature (ta). All data is detrended before analyzing.

169 2.2 Observation and reanalysis datasets

170 The observational and reanalysis data used in this study include: 1) the monthly SST data obtained
 171 from the Hadley Centre Sea Ice and Sea Surface Temperature version 1.1 dataset (HadISST v1,1), with
 172 a horizontal resolution of 1°×1° (Rayner et al., 2003); 2) the monthly, daily, and hourly 10m wind fields
 173 are from the European Centre for Medium-Range Weather Forecasts (ECMWF) reanalysis data Fifth
 174 Generation (ERA5), with a horizontal resolution of 0.25°× 0.25° (Hersbach et al., 2020); 3) the daily
 175 precipitation ~~are is~~ from the Global Precipitation Climate Program version 1.3 (GPCP v1.3), with a
 176 horizontal resolution of 2.5°× 2.5° (Adler et al., 2003); 4) the monthly sea surface wind stress data are
 177 provided by the ECMWF Ocean Reanalysis Data (ORAS5), with a horizontal resolution of 1°× 1° (Zuo
 178 et al., 2019) and America Ocean Data Assimilation Data Set version 2.2.4 (SODA v2.2.4), with a
 179 horizontal resolution of 0.5°× 0.5° (Carton and Giese, 2008); 5) the historical TC data are from the China
 180 Meteorological Administration (CMA) tropical cyclone best track dataset (Ying et al., 2014; Lu et al.,
 181 2021).

182 2.3 Diagnostic framework

183 This study employs a reproducible, model-agnostic diagnostic framework for evaluating resolution-
184 dependent ENSO behavior. Diagnostics include ENSO amplitude and spectrum, ENSO irregularity index,
185 Bjerknes index diagnosis feedback and the corresponding total derivative decomposition, thermocline
186 and current responses, meridional distribution index of zonal wind stress anomaly, oceanic zonal current
187 decomposition, and the high-frequency (HF) atmospheric westerly (easterly) wind index variability and
188 the corresponding noise-to-signal ratio, and TC detection and metrics.

189 Throughout this study, an overbar ($\bar{\cdot}$) denotes the climatological mean field, and a prime (\cdot')
190 denotes the interannual anomaly obtained by removing the climatological seasonal cycle. The subscript
191 'HF' indicates a HF (sub-90-day) filtered field. For example, u'_{HF} denotes the HF component of daily
192 zonal wind anomaly, obtained by applying a 90-day high-pass filter to the daily anomaly field. All
193 symbols are used consistently throughout the paper unless otherwise specified.

194 2.3.1 ENSO amplitude indices, and spectral analysis characteristics and ENSO irregularity index 195 (CVT)

196 Monthly anomalies of Niño3.4 (5°S–5°N, 170°–120°W) SSTA is computed after removing the
197 climatological seasonal cycle. ENSO amplitude is measured by the standard deviation of Niño3.4 index
198 (monthly SSTA averaged in 5°S–5°N, 170°–120°W). Power spectra are derived using the multi-taper
199 method following Thomson (1982). To quantitatively evaluate the regularity of ENSO oscillation, we
200 propose ENSO irregularity is diagnosed via spectral width and cycle-to-cycle variability. an ENSO
201 irregularity index based on the coefficient of variation of inter-event time intervals (CVT). This
202 metric is computed through the following steps.

203 First, ENSO events are identified using the 3-month running mean of the Niño3.4 index. A
204 warm (cold) event is defined when the 3-month running mean Niño3.4 index exceeds 0.5 (falls
205 below –0.5) standard deviation of the Niño3.4 index, and the event is considered to terminate when
206 the Niño3.4 index returns to within the ± 0.5 standard deviation range for at two consecutive months.

207 Second, the time interval between two successive events of the same sign is defined as the time
208 separation between adjacent event peaks (i.e., the month of maximum warming for warm events or
209 maximum cooling for cold events).

210 Third, the CVT is computed as the ratio of the standard deviation to the mean of these inter-

211 event intervals:

$$212 \quad \text{CVT} = \frac{\sigma_T}{\mu_T} \quad (1),$$

213 where T denotes the set of all inter-event intervals, and μ_T and σ_T denote the mean and the
 214 standard deviation of these intervals, respectively.

215 Finally, the CVT is calculate separately for warm events (CVT_{warm}) and cold events (CVT_{cold}),
 216 and their average is taken as the final ENSO irregularity index used in this study. A larger CVT
 217 indicates more irregular ENSO oscillation with highly variable inter-event spacing, whereas a
 218 smaller CVT (approaching zero) indicates a more periodic and regular oscillation.

219 2.3.2 Bjerknes ~~index diagnosis~~~~feedback decomposition~~

220 In order to quantitatively analyze the air-sea coupling processes responsible for ENSO amplitude in
 221 FGOALS-f3 models, the diagnostic framework of BJ index (Kim and Jin, 2011a, 2011b) is performed in
 222 this study. The specific formulation is listed as follows:

$$223 \quad \text{BJ} = \frac{R-\varepsilon}{2} \quad (42),$$

$$224 \quad R = - \left(a_1 \frac{\langle \Delta \bar{u} \rangle_E}{L_x} + a_2 \frac{\langle \Delta \bar{v} \rangle_E}{L_y} \right) - \alpha_s + \mu_a \beta_u \langle -\frac{\partial T}{\partial x} \rangle_E + \mu_a \beta_w \langle -\frac{\partial T}{\partial z} \rangle_E + \mu_a \beta_h a_h \langle \frac{\bar{w}}{H_1} \rangle_E \quad (32),$$

$$225 \quad \frac{\partial \langle h h' \rangle_w}{\partial t} = -\varepsilon \langle h' \rangle_w - F[\tau_x'] - \quad (43),$$

$$226 \quad \langle Q' \rangle_E = -\alpha_s \langle T' \rangle_E \quad (54),$$

$$227 \quad \langle H(\bar{w}) T_{sub}' \rangle_E = a_h \langle T' \rangle_E \quad (65),$$

$$228 \quad \langle h' \rangle_E - \langle h' \rangle_w = \beta_h [\tau_x'] - \quad (76),$$

$$229 \quad \langle H(\bar{w}) w' \rangle_E = \beta_w [\tau_x'] \quad (87),$$

$$230 \quad \langle u' \rangle_E = \beta_u [\tau_x'] + \beta_{uh} \langle h' \rangle_w - \quad (98),$$

$$231 \quad [\tau_x'] = \mu_a \langle T' \rangle_E \quad (109),$$

232 where ~~variables with overbar represent the climatological fields and others denote the anomalous fields~~
 233 ~~obtained by removing the seasonal cycle~~; u , v , and w are the three dimensional oceanic current velocity;
 234 T denotes sea surface temperature ($^{\circ}\text{C}$); $\langle \rangle_E$ and $\langle \rangle_w$ represent averaged volume of the eastern box
 235 region ($5^{\circ}\text{S}-5^{\circ}\text{N}, 170^{\circ}-90^{\circ}\text{W}$) and western box region ($5^{\circ}\text{S}-5^{\circ}\text{N}, 130^{\circ}\text{E}-170^{\circ}\text{W}$), respectively, from the
 236 ocean surface to the mixed layer depth; L_x and L_y denote the longitudinal and latitudinal lengths of the
 237 eastern box, respectively; H_1 ~~indicates~~~~denotes~~ the ~~constant~~-mixed layer depth (two complementary

238 strategies for specifying H_I are adopted in this study and their results are compared in Section 4.1.65m).

239 The coefficients a_1 and a_2 are obtained through linear regression using SST anomalies (SSTA) zonally
240 or meridionally averaged at the boundaries and area-averaged SSTA over the box. the " Δ " in equation (2)
241 represents the differences of ocean current between the eastern and western boundaries. $H(\bar{W}) =$
242 $\begin{cases} 1, \bar{W} > 0 \\ 0, \bar{W} \leq 0 \end{cases}$ is the step function to make sure only upward vertical motion is taken into account. Here, the
243 Equation (1) defines the BJ index, serving as the primary metric for the growth rate examined in this
244 analysis. The corresponding dynamic and thermodynamic feedbacks are expressed in Equation (2). In
245 equation (3), the first term on the right-hand side ~~are~~ is the damping process at the rate of ε ; the second
246 term represents the Sverdrup transport across the equatorial Pacific basin. In Equations (4) to (9), α_s (s-
247) indicates the response of the thermodynamic damping to SSTA; μ_a (N m⁻² K⁻¹) represents the response
248 of surface wind stress anomalies (τ_x') to SSTA; β_u (m s⁻¹ (N m⁻²)⁻¹) represents the response of upper
249 ocean current anomalies (u_o') to τ_x' ; β_h (m (N m⁻²)⁻¹) indicates the response of the anomalous zonal
250 slope of the equatorial Pacific thermocline to τ_x' ; β_w (m s⁻¹ (N m⁻²)⁻¹) denotes the response of ocean
251 upwelling anomalies (w_o') to τ_x' ; a_h (K m⁻¹) shows the effect of thermocline depth change on
252 subsurface temperature anomalies. ~~In this study, the computational region is (5°S–5°N, 130°E–90°W).~~

253 Based on the above equations, the main contributing terms of the BJ index include two negative
254 feedback processes: the dynamic damping by mean advection (MA; $-\left(a_1 \frac{\langle \Delta \bar{u} \rangle_E}{L_x} + a_2 \frac{\langle \Delta \bar{v} \rangle_E}{L_y}\right)$), the
255 thermodynamic feedback (TD; $-\alpha_s$), and three positive feedback processes: the zonal advection
256 feedback (ZA; $\mu_a \beta_u \langle -\frac{\partial \bar{T}}{\partial x} \rangle_E$), the thermocline feedback (TH; $\mu_a \beta_h a_h \langle \frac{\bar{w}}{H_1} \rangle_E$), and the Ekman feedback
257 (EK; $\mu_a \beta_w \langle -\frac{\partial \bar{T}}{\partial z} \rangle_E$).

258 2.3.3 Meridional distribution index

259 To further quantify the meridional structure of ENSO-related τ_x' , a meridional distribution index
260 (MDI) that was proposed by Chen et al. (2015b), is employed. The MDI is defined as:

$$261 \quad \text{MDI} = \frac{\int_{-10^\circ}^{10^\circ} \tau_x'(y) |y| dy}{\int_{-10^\circ}^{10^\circ} \tau_x'(y) dy} \quad (11),$$

262 where y denotes latitude, and $\tau_x'(y)$ represents the meridional profile of the normalized τ_x' . The
263 normalized τ_x' obtained by regressing the zonal wind stress anomaly field onto the Niño4 region (5°S–
264 5°N, 160°E–150°W) averaged zonal wind stress anomalies and then averaged over the Niño4 longitude

range (160°E–150°W). The MDI provides a quantitative measure of the meridional concentration of ENSO-related τ_x' within the equatorial band. Specifically, a smaller MDI indicates that τ_x' is more concentrated near the equator, whereas a larger MDI indicates a broader meridional distribution.

2.3.4 Oceanic zonal current decomposition

ENSO-related zonal current anomaly (u_o') in the equatorial region is composed of anomalous zonal geostrophic currents (u_g') and anomalous Ekman currents (u_e') (Su et al., 2010; Su et al., 2014). The specific formulas of u_g' and u_e' are listed below:

$$u_g' = -\frac{g\partial^2 D'}{\beta\partial y^2} \quad (12),$$

$$u_e' = \frac{1}{\rho H_l} \frac{r_s \tau_x' + \beta y \tau_y'}{r_s^2 + (\beta y)^2} \quad (13),$$

where β and r_s are the planetary vorticity gradient and Rayleigh dissipation rate (0.5 day⁻¹), respectively; τ_y' denotes the sea meridional wind stress anomaly; H_l denotes the mean mixed layer depth, and ρ is the seawater density.

2.3.3-5 HF westerly (easterly) wind index and noise-to-signal ratio

An index regarding the HF zonal wind anomalies is used to quantitatively measure the intensity of HF westerly (easterly) wind activity in the f3-L and f3-H models. This index (named WWI index and EWI index) is defined as the integration of the averaged zonal HF westerly (easterly) wind over a fixed region (5°S–5°N, 120°E–180°). The formula is as follows:

$$WWI \text{ index} = \int_{time1}^{time2} u_{HF}' dt, \quad u_{HF}' > 1m/s \quad (14),$$

$$EWI \text{ index} = \int_{time1}^{time2} u_{HF}' dt, \quad u_{HF}' < -1m/s \quad (15),$$

where u_{HF}' represents the daily zonal wind anomaly after applying a 90-day high-pass filter, *time1* and *time2* represent the start and end time of the integrated period, respectively. In this study, the development period of ENSO event (January to August) is selected as the integrated period.

A noise-to-signal ratio (NSR) metric is proposed to quantify the relative magnitude of stochastic atmospheric forcing compared to the ENSO signal. The NSR is defined as:

$$NSR = \frac{\sigma(u_{HF}')}{\sigma(SSTA_{Ni\tilde{n}03.4})} \quad (16),$$

291 where $\sigma(u'_{HF})$ is the standard deviation of 90-day high-pass-filtered zonal wind anomalies averaged over
292 the western equatorial Pacific (5°S – 5°N , 120°E – 180°), and $\sigma(SSTA_{Ni\tilde{no}3.4})$ denotes the standard deviation
293 of Niño3.4 index. A larger *NSR* indicates stronger stochastic forcing relative to the ENSO signal, and
294 vice versa.

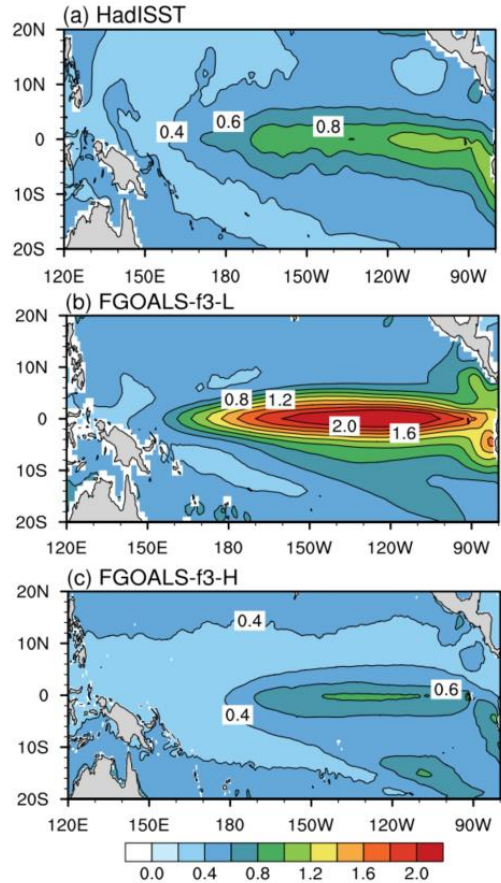
295 **2.3.56 TC detection and metrics**

296 The TC detection algorithm developed by the Geophysical Fluid Dynamics Laboratory
297 (<https://www.gfdl.noaa.gov/tstorms/>; Zhao et al., 2023) was used to detect TC activities in FGOALS-f3
298 model. The basic identification criteria and steps are: 1) a local minimum SLP is found within a maximum
299 distance of 3,000 km; 2) the wind speed at 850 hPa for this vortex exceed 17 m/s; 3) the absolute value
300 of the vorticity is greater than $1.5 \times 10^{-4} \text{ s}^{-1}$; 4) The temperature within 1200 km of the vortex center is
301 higher than that in the 1200-2400 km radius at 300-500 hPa, indicating a warm core structure; 5) The
302 lifespan of this TC should be at least three days (72h).

303 We further employ two metrics, i.e., accumulated cyclone energy (ACE) and TC track density
304 (TCTD), to assess the TC activity in FGOALS-f3 models. The ACE index (Bell et al., 2000) in each grid
305 cell is defined as the sum of the squares of the maximum surface wind speeds for all TCs occurring within
306 a $4^{\circ} \times 4^{\circ}$ grid cell over all 6-hourly periods (i.e., $ACE = \sum_i V_{max}^2$, where i denotes the i th TC in a grid cell
307 and V_{max} denotes its maximum surface wind speed). The TCTD in each grid is defined as the sum of the
308 number of TCs that have passed through the region within a distance of $4^{\circ} \times 4^{\circ}$ from the grid center.

309 **3. Evaluation of ENSO Characteristics in f3-L and f3-H**

310 Figure 1 shows the spatial distribution of the standard deviation (STD) of SSTA over the tropical
311 Pacific. In both the high- and low-resolution versions of FGOALS-f3, the interannual variability of SSTA
312 is concentrated in the central-eastern equatorial Pacific (Fig. 1b-c), which is spatially consistent with the
313 observation (Fig. 1a). However, significant differences exist in the ENSO amplitude. Specifically, the
314 STD of the Niño3.4 index is 0.67 $^{\circ}\text{C}$ in the observation, 1.53°C in f3-L, and 0.62°C in f3-H, respectively.
315 This indicates that f3-L severely overestimates the ENSO amplitude, whereas f3-H's simulation is much
316 closer to the observation. Considering that the ENSO amplitude simulated in f3-L is approximately 2.5
317 times that of f3-H, this study will firstly address the causes of the stronger ENSO amplitude in f3-L
318 compared to its counterpart in f3-H.

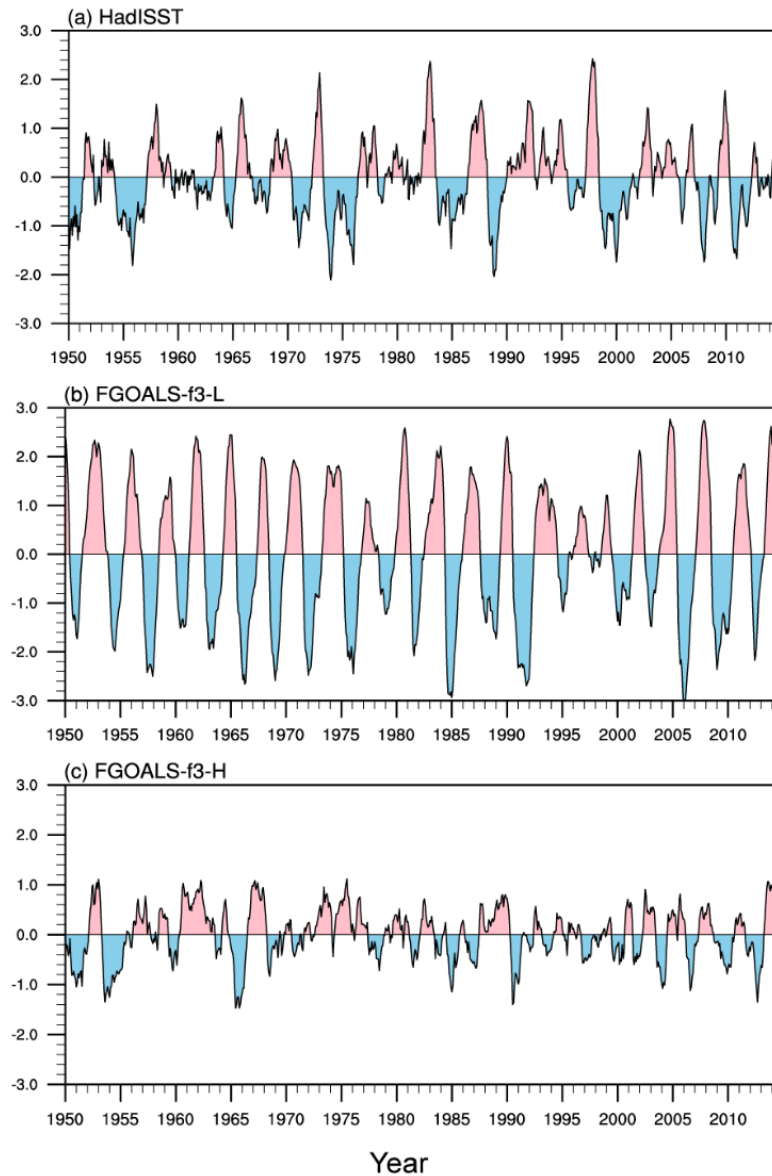


319
320
321

Figure 1. The standard deviation of SSTA (shading, units: °C) for (a) Observation (HadISST), (b) f3-L and (c) f3-H.

322
323
324
325
326
327
328
329
330
331

Figure 2 presents the time series of the Niño3.4 index for the observation and the two model versions. Obviously, the oscillation intensity of Niño3.4 index in f3-L is much stronger than that in the observation and f3-H, consistent with the results of the STD analysis (Fig. 1). Another notable difference lies in the regularity of the oscillation: ENSO events in f3-L exhibit highly periodic behavior, with a regular transition between warm and cold phases. In contrast, the ENSO evolution in both the observation and f3-H exhibit obvious irregularity. Furthermore, we conduct the power spectrum analysis on the Niño3.4 indices (Fig. 3). In the observation, the power spectrum is characterized by a broad band of 2–8 years. However, the power spectrum in f3-L shows a sharp and significant unimodal peak at approximately 3-year period, with excessive concentration of ENSO energy at this dominant period. In contrast, f3-H reproduces a broadband spectral distribution similar to the observation.



332

333 **Figure 2.** Temporal evolution of Niño3.4 index (the averaged SSTA in the Pacific Niño3.4 region (5°S–5°N, 170°W–
 334 120°W), units: °C) for (a) Observation (HadISST), (b) f3-L and (c) f3-H.

335

336

337

338

339

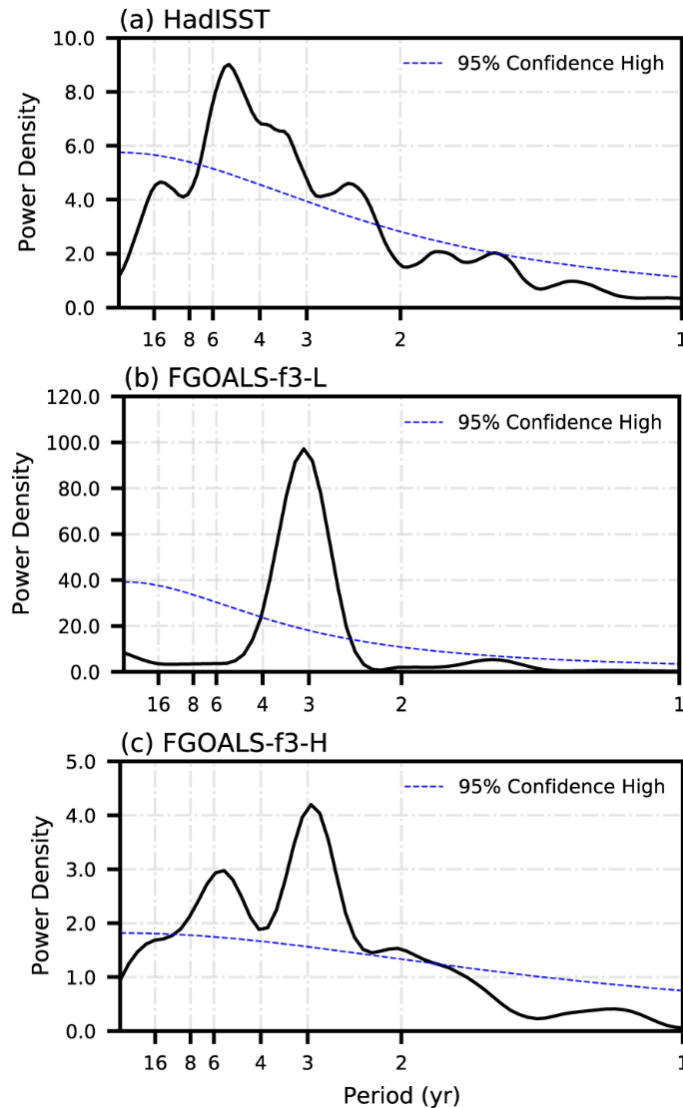
340

341

Based on the proposed ENSO irregularity index, we calculated the CVT for the observation, f3-L and f3-H. As shown in Table 2, the CVT values are 0.61, 0.17, and 0.53 for the observation, f3-L and f3-H, respectively. The results clearly indicate that ENSO oscillation in f3-L is excessively regular compared to the observation (CVT of 0.17 vs. 0.61), whereas f3-H produces a degree of irregularity much closes to the observation. Therefore, the second question this study will address is: what causes the overly regular oscillation in f3-L, while f3-H captures more realistic irregularity?

Table 2. The ENSO irregularity index (CVT) for the observation, f3-L and f3-H.

<u>Observation</u>	<u>f3-L</u>	<u>f3-H</u>
--------------------	-------------	-------------



343

344

345

Figure 3. The power spectra of Niño3.4 index for (a) Observation (HadISST), (b) f3-L and (c) f3-H. The blue line in the plots is the 95% confidence level.

346

4. Process-based Diagnosis of ENSO Amplitude Differences

347

4.1 Diagnostic analysis based on the BJ index

348

349

350

351

352

353

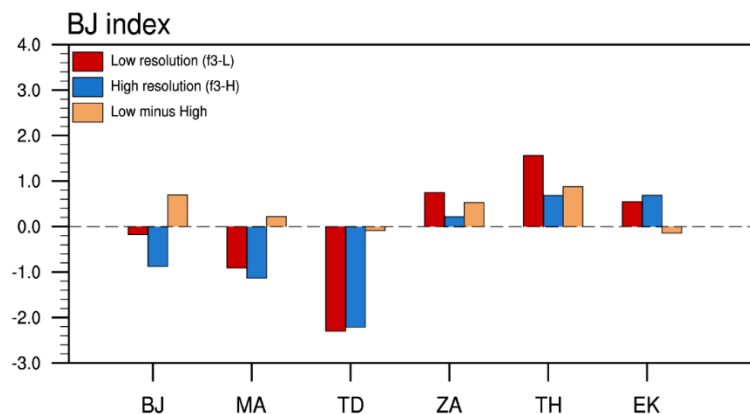
354

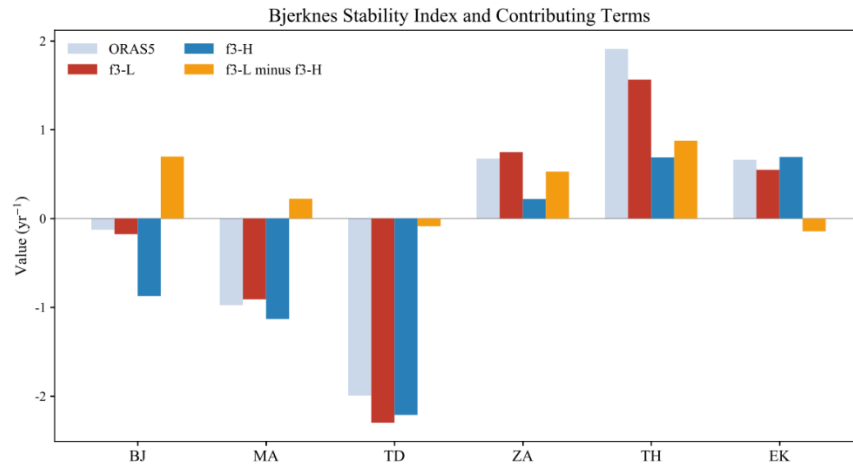
To investigate the physical mechanisms responsible for the ENSO amplitude difference between the high- and low-resolution versions, we apply the BJ index framework to quantitatively diagnose the stability of the coupled ocean-atmosphere system in both models. When applying the BJ index or the commonly used mixed-layer heat budget diagnosis, one practical issue is the choice of mixed layer depth (MLD) and whether the results are sensitive to this choice. We therefore first examine the spatial distribution of the climatological MLD in f3-L and f3-H. Here the MLD is defined as the depth at which the ocean temperature is 0.8°C lower than the SST, following Wang et al. (2012) and Chen et al. (2016b).

As shown in Figure S1, the climatological MLD exhibits a pronounced zonal variation along the equatorial Pacific: it is relatively shallow in the far eastern Pacific and gradually deepens toward the central equatorial Pacific. Moreover, the MLD differs between the two model versions, with the eastern box-mean values of approximately 65 m in f3-L and 50 m in f3-H over the eastern equatorial Pacific (i.e., the eastern box used in the BJ index calculation). Given this zonal and inter-model variability, we adopt two complementary MLD strategies in the BJ index diagnostic.

Strategy 1 (Constant MLD): A fixed MLD of a constant value is applied to both f3-L and f3-H when computing the BJ index. This approach follows the conventional practice in previous BJ index studies (e.g., Kim and Jin, 2011a, 2011b; Chen et al., 2019a, 2019b) and facilitates a direct comparison between the two simulations under an identical diagnostic framework. From the perspective of the BJ-index eastern-box average, the climatological mean MLD over the eastern equatorial Pacific is approximately 65 m in f3-L and 50 m in f3-H. Therefore, in this first approach, we use a constant value of 65 m for both simulations.

The BJ index results under Strategy 1 are shown in Figure 4. Figure 4 presents the BJ index calculated using a fixed MLD of 65 m and its five contributing terms for the reanalysis, f3-L and f3-H, as well as their difference (f3-L minus f3-H). The results demonstrate that, although both models show yield negative BJ indices, the index-value for f3-L is significantly larger (i.e., a smaller less negative-value) than that for f3-H model. According to the physical interpretation of the BJ index (Jin et al., 2006; Kim and Jin, 2011a; Kim and Jin, 2011b), a smaller absolute value of the less negative BJ index in f3-L indicates that the coupled air-sea system in f3-L is more unstable than that in f3-H. This more unstable coupled system in f3-L is more favorable for ENSO's growth-rate, thereby leading to a stronger ENSO amplitude in f3-L than that in f3-H.





378

379 **Figure 4.** BJ index and the corresponding main contributing terms for the reanalysis (ORAS5; grey bars), the f3-L
 380 (red bars), f3-H (blue bars) and their difference (f3-L minus f3-H, orange bars). Here the BJ index is calculated using
 381 a fixed MLD of 65 m. The five contributing terms including dynamic damping by mean advection feedback (MA),
 382 thermodynamic damping feedback (TD), zonal advection feedback (ZA), thermocline feedback (TH) and Ekman
 383 feedback (EK).

384 It is worth noting that the BJ index derived from the reanalysis is not more negative than that of f3-
 385 L, despite the observed ENSO amplitude being slightly weaker than that simulated by f3-L. This
 386 inconsistency can be attributed to two factors. First, reanalysis products carry inherent uncertainties, and
 387 direct comparison between reanalysis-derived and model-derived BJ indices should be interpreted with
 388 caution. Second, the BJ index is a linear diagnostic framework that does not account for nonlinear
 389 processes, including nonlinear atmospheric responses, semi-stochastic atmospheric noise (i.e., the HF
 390 zonal wind anomalies discussed in this study), and oceanic nonlinear processes such as nonlinear
 391 dynamical heating (Wei et al., 2026). In other words, while the BJ index is a useful tool for assessing
 392 whether the linear air–sea coupling framework favors ENSO growth, the actual ENSO amplitude is
 393 jointly determined by linear coupling, nonlinear processes, and stochastic forcing. This represents an
 394 inherent limitation of the BJ index framework. Therefore, a comprehensive evaluation of ENSO
 395 simulation requires not only the BJ index analysis of linear feedback processes but also diagnostics
 396 beyond the linear framework to assess the roles of nonlinear processes and stochastic forcing, as
 397 addressed in Section 5 of this study. In the following, our primary focus is on examining the differences
 398 in the BJ index and its contributing terms between f3-L and f3-H.

399 A further question arises: which physical processes contribute to the more unstable coupled system
 400 in f3-L? By examining the differences in the five contributing terms of the BJ index (orange bars in Fig.
 401 4), we find that the differences in the thermocline feedback (TH) term and the zonal advection feedback

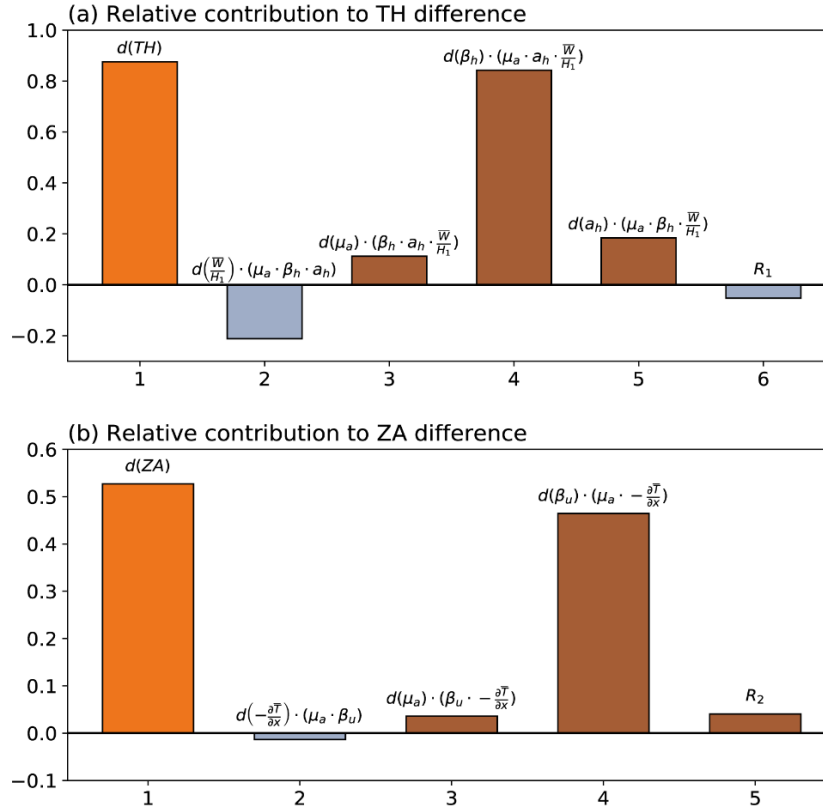
402 (ZA) term are the ~~decisive factors driving the difference in dominant contributors to~~ the BJ index
403 ~~difference~~ (i.e., the system stability) between the ~~high- and low-resolution FGOALS-f3two model~~
404 versions. Therefore, the ~~following subsequent~~ analysis will focus on the physical mechanisms
405 responsible for the stronger TH and ZA terms in f3-L relative to f3-H.

406 **Strategy 2 (Longitude-varying MLD):** Each model version uses its own longitude-dependent
407 climatological MLD (averaged over the equatorial band, 5°S–5°N) when computing the BJ index. This
408 approach accounts for zonal variations and inter-model differences in stratification, providing a more
409 physically realistic diagnostic. In this approach, when calculating the BJ index, we diagnose the mixed-
410 layer temperature anomaly above the longitudinally varying climatological MLD (Figure S1) within the
411 three-dimensional eastern equatorial Pacific box.

412 Figure S2 presents the BJ index and its contributing terms calculated using the longitude-varying
413 MLD for the reanalysis, f3-L, and f3-H, as well as their difference (f3-L minus f3-H). The main results
414 are broadly consistent with those obtained under Strategy 1. Specifically, the BJ index of f3-H remains
415 more negative than that of f3-L, which largely explains the weaker ENSO amplitude in f3-H; and the BJ
416 index difference between the two models is still primarily attributable to the TH and ZA terms. The only
417 notable discrepancy between the two strategies lies in the MA term, which represents the dynamic
418 damping by mean zonal and meridional advection. In brief, under the longitude-varying MLD strategy,
419 the shallower MLD in f3-H means that the vertical averaging is taken over a thinner layer, in which the
420 poleward (damping) branch dominates more strongly, resulting in a more negative MA term in f3-H
421 compared to f3-L. A detailed analysis regarding the MA difference between f3-H and f3-L is provided in
422 the supplementary material. Overall, the sensitivity test demonstrates that the core conclusions of the BJ
423 index analysis, namely, the more unstable coupled system in f3-L and the dominant roles of the TH and
424 ZA terms are robust across both MLD strategies.

425 According to the definition of the BJ index (see Eq. (23)), each ocean dynamic term consists of two
426 components: one related to the mean state and the other to air-sea feedback processes. Considering that
427 both components may contribute to the differences in ~~ocean dynamic~~ the TH and ZA terms between f3-L
428 and f3-H, we ~~first~~ calculate the relative contributions of each component to the total difference ~~in the TH~~
429 ~~and ZA terms~~ using a total derivative decomposition. As shown in Figure 5a, the stronger TH term in f3-
430 L compared to f3-H (bar 1) primarily ~~comes-arises~~ from the difference in β_h (bar 4). The differences in
431 μ_a and a_h ~~feedback processes~~ make minor contributions, while the mean state differences and the
432 covariance term make negative contributions. Thus, the dominant factor ~~causing~~ responsible for the
433 stronger TH term in f3-L is the difference in β_h . Similarly, for the stronger ZA term in f3-L, the results
434 (Fig. 5b) show that the difference in ~~the~~ ZA term (bar 1) is primarily determined by the difference in β_u

(bar 4), while the difference in a_h and the covariance change-term have marginal contributions.

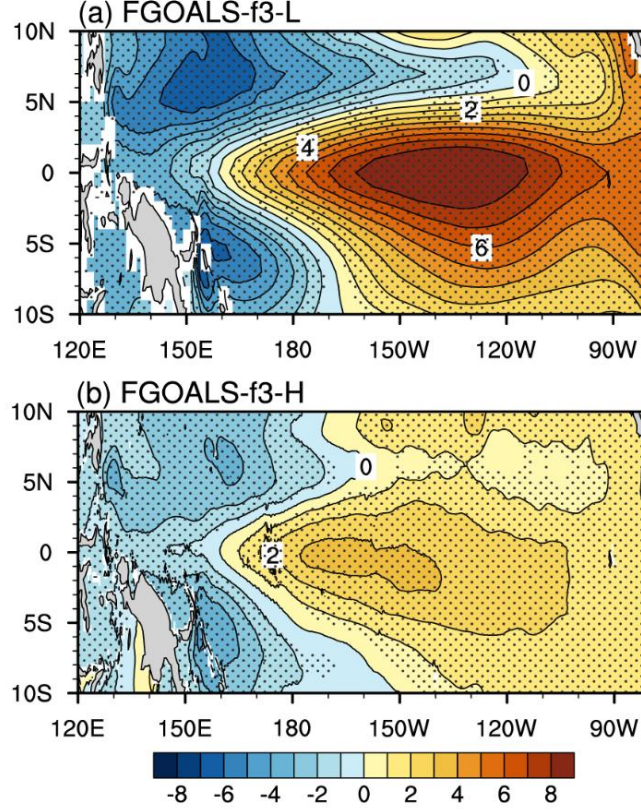


436

437 **Figure 5.** (a) The contributions of each terms different components to the change in the thermocline feedback (TH)
 438 term. Bar 1 indicates the change of in TH term [f3-L minus f3-H, $d(TH)$]. Bar 2 denotes the contribution from the
 439 mean state part change [$d(\bar{w}/H_1)$] to the change of in TH term. Bar 3, Bar 4 and Bar 5 indicate the contributions
 440 from the air-sea feedbacks [$d(\mu_a)$, $d(\beta_h)$ and $d(a_h)$] to the change of in TH feedback term, respectively. Bar 6 is the
 441 residual, which denotes the contribution from the covariant changes of both the mean state part and the air-sea
 442 feedbacks. (b) The contribution of each terms in the same as (a) but for the zonal advection feedback (ZA). Bar 1
 443 indicate the change of in ZA term [f3-L minus f3-H, $d(ZA)$]. Bar 2 denotes the contribution from the mean state part
 444 change [$d(-\frac{\partial \bar{T}}{\partial x})$] to the change in of TH-ZA term. Bar 3 and Bar 4 indicate the contributions from the air-sea
 445 feedbacks [$d(\mu_a)$ and $d(\beta_u)$] to the change of ZA feedback, respectively. Bar 5 is the residual, which
 446 denotes representing the contribution from the covariant changes of both the mean state part and the air-sea feedbacks.

447 4.2 Resolution dependence of the β_h feedback process difference

448 The air-sea feedback process β_h represents the response of the equatorial Pacific thermocline tilt
 449 to τ_x' . Figure 6 shows the regression of thermocline depth anomalies onto zonal wind stress anomalies
 450 for the two models. Both models reproduce the expected pattern: in response to positive τ_x' over the
 451 equatorial Pacific, the anomalous thermocline depth (D') deepens in the eastern equatorial Pacific and
 452 shoals in the western equatorial Pacific. However, the response is much stronger in f3-L than in f3-H.



453
 454 **Figure 6.** Distribution of the response of thermocline depth anomaly to zonal wind stress anomaly [β_h ; units: $\text{m} (\text{N m}^{-2})^{-1}$] for (a) f3-L and (b) f3-H. Based on the linear relationship between sea surface height anomaly (SSHA) and
 455 thermocline depth anomaly (D'), the SSHA is used as a proxy of D' . The D' response to zonal wind stress anomaly
 456 is derived through regressing the SSHA field onto the averaged zonal wind stress anomaly over equatorial Pacific
 457 (5°S – 5°N , 120°E – 100°W). The stippling in this plot denotes the regression coefficient exceeding a confidence level
 458 of 99% by using Student's t test.
 459

460 Based on the Sverdrup balance relationship (Jin, 1997; Li, 1997), the response of the D' to τ_x' is
 461 primarily determined by the mean equatorial thermocline depth (\bar{H}) and τ_x' :

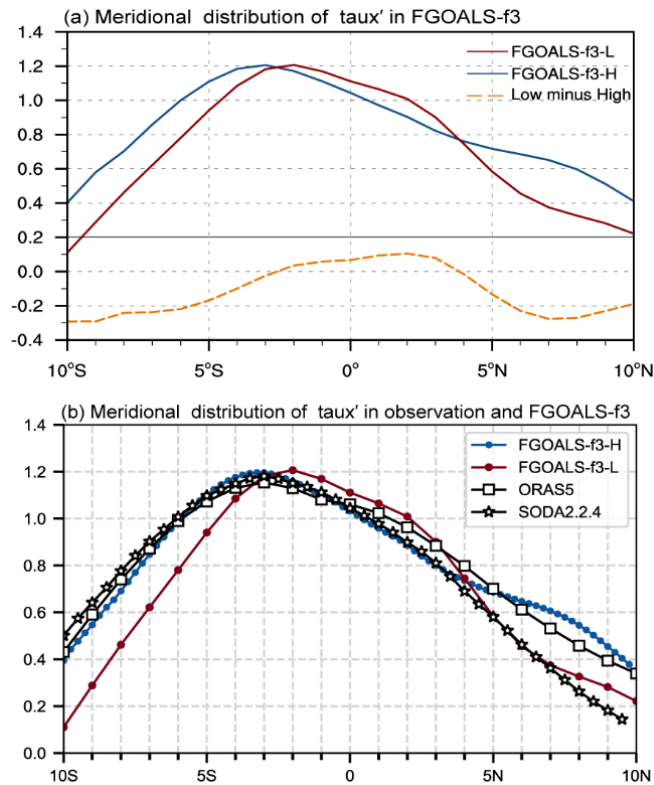
462
$$\frac{\partial D'}{\partial x} = \frac{\tau_x'}{\rho g \bar{H}} \quad (147),$$

463 where ρ is the seawater density and g is the reduced gravity. We first examine the mean thermocline
 464 depth in both models and find that the difference in \bar{H} between f3-L and f3-H is negligible (figure not
 465 shown). Therefore, the difference in \bar{H} is not the primary cause.

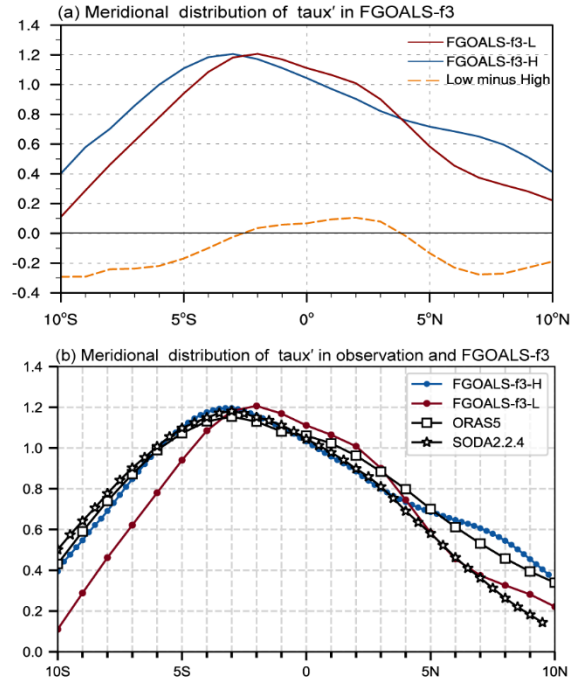
466 Previous studies (Chen et al., 2015b; Chen et al., 2019a) have pointed out that the meridional
 467 structure of τ_x' is another key factor influencing the strength of β_h . Figure 7a presents the meridional
 468 structure of τ_x' for the two models and their difference (orange, f3-L minus f3-H). A significant
 469 difference exists: although the regression results show the same magnitude of τ_x' within the equatorial
 470 Pacific (5°S – 5°N), the τ_x' in f3-L is meridionally more concentrated near the equator (0°) than that in

471 f3-H. Since the τ_x' closer to equator is more effective in influencing D' (Chen et al., 2015b; Chen et al.,
 472 2019a), this more equatorially-confined meridional structure of τ_x' in f3-L inevitably results in a
 473 stronger response of D' to τ_x' (i.e., a larger β_h).

474 Furthermore, we compare the meridional structure of ENSO-related τ_x' in the two model versions
 475 with two reanalysis datasets. As shown in Fig. 7b, the meridional structures of τ_x' in the two reanalysis
 476 products (black lines) are very similar between 10°S–5°N, while some discrepancies exist within 5°N–
 477 10°N region. For the models, the f3-H (25 km atmospheric resolution) shows a τ_x' meridional structure
 478 in the equatorial region (5°S–5°N) that substantially resembles both reanalysis datasets. In contrast, the
 479 meridional structure of τ_x' within 5°S–5°N in f3-L (100 km atmospheric resolution) shows obvious
 480 discrepancies from the two reanalysis datasets. This suggests that model horizontal resolution can
 481 influence ENSO simulation by affecting the meridional distribution of τ_x' . The higher horizontal
 482 resolution is conducive to the more realistic representation of equatorial τ_x' meridional structure,
 483 thereby yielding a more reasonable thermocline feedback and ENSO amplitude.



484

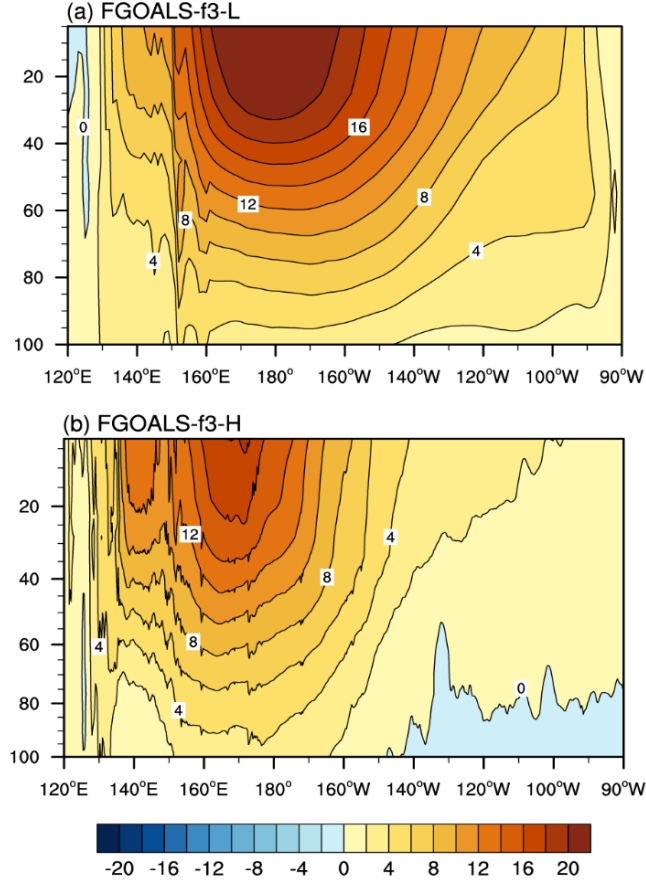


485

486 **Figure 7.** Meridional structure of normalized zonal wind stress anomalies [units: $\text{N m}^{-2} (\text{N m}^{-2})^{-1}$] averaged over the
 487 Niño4 longitude range (160°E – 150°W) for (a) the result of f3-L (red solid line), f3-H (blue solid line) and their
 488 difference (orange dash line, f3-L minus f3-H). In this plot, all the data are both interpolated onto a $1^\circ \times 1^\circ$ grid to
 489 facilitate the comparison; (b) the results of ORAS5 (black line marked by square, with a $1^\circ \times 1^\circ$ grid), SODA2,2,4
 490 (black line marked by asterisk, with a $0.25^\circ \times 0.25^\circ$ grid), f3-L (red line marked by circle, with a $1^\circ \times 1^\circ$ grid) and
 491 f3-H (blue line marked by circle, with a $0.25^\circ \times 0.25^\circ$ grid). The normalized zonal wind stress anomalies are obtained
 492 by regressing the zonal wind stress anomalies field onto the Niño4 region (5°S – 5°N , 160°E – 150°W) averaged zonal
 493 wind stress anomalies.

494 **4.3 Resolution dependence of the β_u feedback process**

495 The air-sea feedback process β_u represents the response of the equatorial Pacific upper ocean zonal
 496 current anomaly (u'_o) to τ'_x . Figure 8 shows the equatorial profile for the response of u'_o to τ'_x in both
 497 models. Both models simulate eastward u'_o a unit eastward τ'_x in equatorial Pacific, but the response
 498 is significantly stronger in f3-L than in f3-H.



499

500

501

502

503

Figure 8. Vertical profile (averaged over 5°S–5°N) of the response of zonal ocean current anomaly (u'_o) to the zonal wind stress anomaly [β_u ; units: $\text{m s}^{-1} (\text{N m}^{-2})^{-1}$] for (a) f3-L and (b) f3-H. The u'_o response to zonal wind stress anomaly is derived through regressing the u'_o field onto the averaged zonal wind stress anomaly over equatorial Pacific (5°S–5°N, 120°E–100°W).

504

505

506

507

508

509

510

511

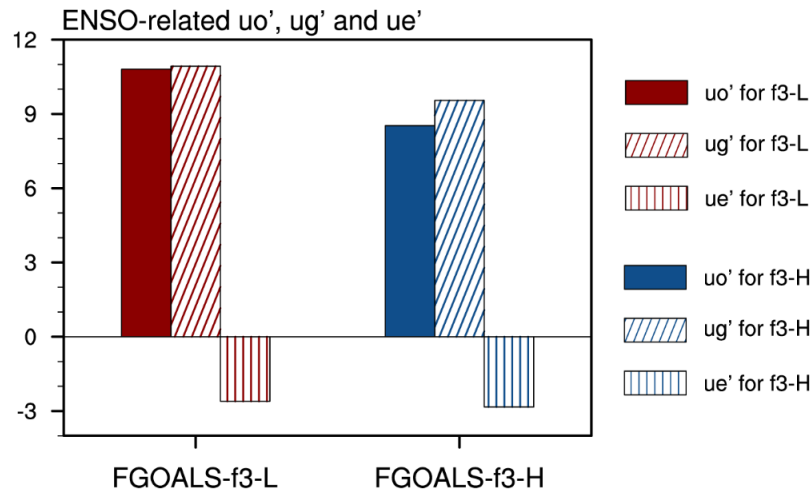
512

513

514

Considering that ENSO-related u'_o in the equatorial region is composed of anomalous zonal geostrophic currents (u'_g) and anomalous Ekman currents (u'_e) (see Section 2.3.4), we first diagnose the response of u'_g and u'_e to wind stress anomalies (Fig. 9). In both versions, the response of u'_o to τ'_x is primarily contributed by the response of u'_g to τ'_x , while the contribution of u'_e is much smaller. This indicates that the difference in u'_g response to τ'_x is the main cause of the difference in β_u between the two model versions. Based on the geostrophic formula (Eq. (12)), the magnitude of u'_g is related to the second-order meridional derivative of D' . Since the meridional structure of D' (Figure 6) exhibits a parabolic shape (peaking at equator and decreasing poleward), a stronger D' in the equatorial region corresponds to a larger value of second-order meridional derivative ($-\frac{\partial^2 D'}{\partial y^2}$) and, consequently, a stronger u'_g . As the D' response to τ'_x is primarily modulated by the $\beta_{\bar{h}}$ process, the difference in the β_u between the f3-L and f3-H is also primarily attributed to difference in the $\beta_{\bar{h}}$ process. That is, the

515 stronger $\beta_{\tilde{h}}$ in f3-L leads to a stronger D' , which in turn induces a stronger u'_g and u'_o and ultimately
 516 resulting in a stronger β_u .



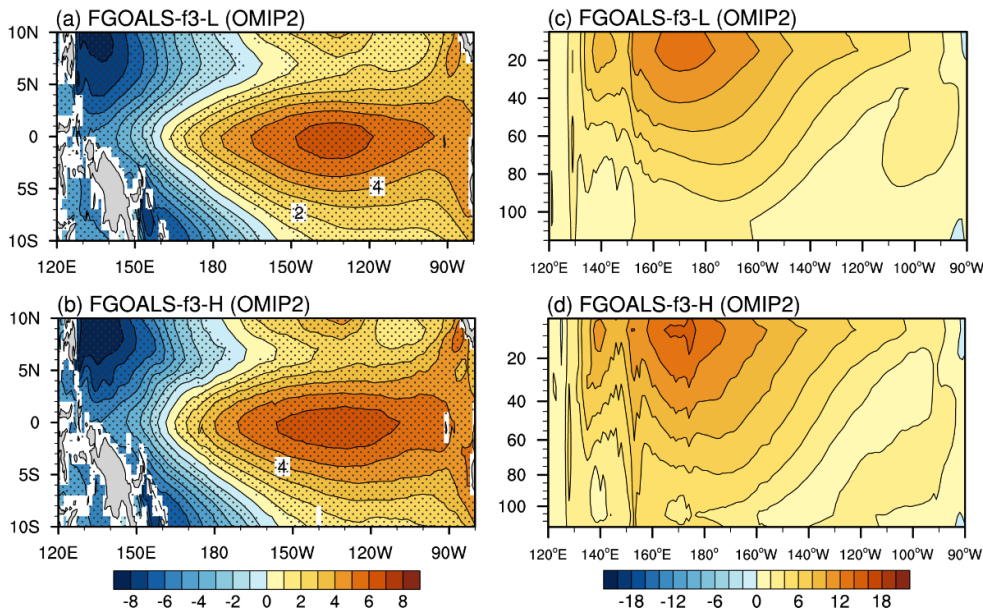
517
 518 **Figure 9.** The ENSO-related zonal current anomalies (u') averaged over 0–65m, zonal geostrophic current anomalies
 519 (u_g') and zonal Ekman current anomalies (u_e') along the equatorial eastern Pacific (2°S–2°N, 180°–80°W) for f3-L
 520 (red bar) and f3-H (blue bar). The ENSO-related zonal current anomalies, zonal geostrophic current anomalies and
 521 zonal Ekman current anomalies are obtained by regressing it anomalies field onto the zonal wind stress anomalies
 522 averaged over Niño4 region (5°S–5°N, 160°E–150°W), respectively.

523 4.4 Comparison with OMIP simulations

524 It should be noted that although our conclusions drawn from Coupled General Circulation Model
 525 (CGCM) indicate that the improved ENSO simulation is closely linked to the increased atmospheric
 526 resolution, the potential influence of oceanic horizontal resolution on ENSO simulation also merits brief
 527 examination. For instance, from the perspective of the oceanic component of CGCM (OGCM), Li et al.
 528 (2025) examined the oceanic zonal current and thermocline depth anomalies to zonal wind forcing by
 529 analyzing the outputs from Ocean Model Intercomparison Project 2 (OMIP2, Griffies et al. 2016) and
 530 found that the oceanic response to wind forcing is a key factor influencing ENSO simulation. Therefore,
 531 the resolution-induced contrast between the OMIP experiment and the CMIP experiment (i.e., the
 532 “historical” experiment) is a noteworthy phenomenon that warrants explanation.

533 According to the CMIP6’s protocol, OMIP2 experiments are forced by the identical atmospheric
 534 reanalysis datasets, thus providing an ideal framework to isolate biases originating from the oceanic
 535 component. Both f3-L and f3-H have participated in OMIP2, with respective oceanic horizontal
 536 resolutions of approximately 1° and 0.1°. To further assess the potential impact of oceanic horizontal
 537 resolution on ENSO simulation, we compare the key air-sea feedback terms ($\beta_{\tilde{h}}$ and β_u) between f3-L

538 and f3-H OMIP2 outputs. As shown in figure 10, the response of zonal current and thermocline depth
 539 anomalies to the identical τ'_x are remarkably similar between the two ocean models. This indicates that
 540 the differences in OGCM resolution itself may not be ~~not~~ the primary driver of the differences in β_h and
 541 β_u . Moreover, this finding (Fig. 10) stands in stark contrast to the large differences in β_h and β_u
 542 identified in the two coupled simulations (Figures 6 and 8). ~~Therefore, the evidence from the OMIP2~~
 543 ~~experiments corroborates our main conclusion: the refined atmospheric horizontal resolution, which more~~
 544 ~~realistically captures the meridional structure of τ'_x , plays a decisive role in improving the simulation of~~
 545 ~~the key air-sea feedbacks (β_h and β_u) and ENSO amplitude in FGOALS-f3 model. Nevertheless, a more~~
 546 ~~comprehensive investigation, potentially involving finer oceanic resolutions and their interactions with~~
 547 ~~the atmosphere, deserves further exploration in the future.~~



548
 549 **Figure 10.** (a)–(b) and (c)–(d) are same as Figure 6 and 8, respectively, but for the OMIP2 simulations.

550 To understand the contrasting OMIP–CMIP behavior, we compare the meridional structures of the
 551 “normalized τ'_x ” between the CMIP and OMIP experiments for both model versions, as shown in Figure
 552 S5. Here the normalized τ'_x is obtained by regressing the τ'_x field onto Niño4-region-averaged τ'_x ,
 553 and then averaging over the Niño4 longitude range (160°E–150°W). This normalization procedure
 554 enables a fair comparison of the meridional structure of τ'_x across different experiments and model
 555 versions. In f3-L, the CMIP experiment produces stronger τ'_x near the equator compared to the OMIP
 556 forcing that was derived from the JRA55-do reanalysis (red lines in Fig. S5). This leads to an enhanced
 557 thermocline response in CMIP relative to OMIP. Conversely, in f3-H, the CMIP experiment yields

weaker equatorial τ_x' than the OMIP forcing (blue lines in Fig. S5), resulting in a weaker thermocline response in CMIP relative to OMIP.

Table 3. Meridional distribution index (MDI; units: $^{\circ}$) of τ_x' , calculated from the meridional structure of normalized τ_x' as shown in Fig. B6.

	f3-L	f3-H
CMIP	2.55	2.71
OMIP	2.68	2.64

Furthermore, we quantify these structural differences in τ_x' between the CMIP and OMIP experiments based on the MDI metric, as introduced in section 2.3.3. The qualitative differences in τ_x' distributions shown in Fig. S5 are corroborated by the MDI results (Table 3). In f3-L, the CMIP experiment yields a notably smaller MDI (2.55°) than the OMIP experiment (2.68°), indicating a more equatorially concentrated τ_x' structure that can more efficiently drive thermocline variability, and hence produces a larger β_h in the CMIP experiment. Conversely, in f3-H, the CMIP experiment exhibits a larger MDI (2.71°) than the OMIP experiment (2.64°), corresponding to a broader τ_x' distribution that drives a more moderate thermocline response and a smaller β_h .

Therefore, the evidence from the OMIP2 experiments corroborates our main conclusion: the refined atmospheric horizontal resolution, which more realistically captures the meridional structure of τ_x' , plays a decisive role in improving the simulation of the key air-sea feedbacks (β_h and β_u) and ENSO amplitude in FGOALS-f3 model. Nevertheless, a more comprehensive investigation, potentially involving finer oceanic resolutions and their interactions with the atmosphere, deserves further exploration in the future.

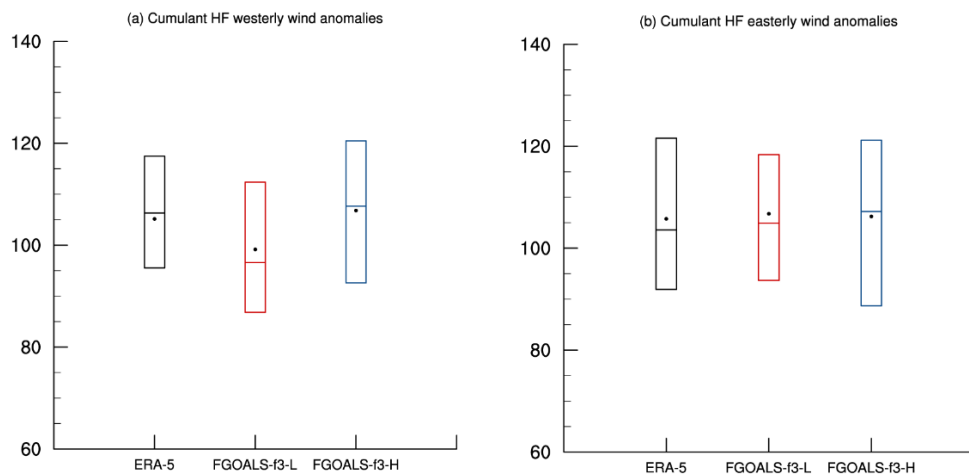
5. Diagnostic of Oscillation Regularity

5.1 Resolution dependence of ENSO irregularity: Differences in HF wind activity

A large body of studies have suggested that the HF zonal wind activity over the western and central equatorial Pacific (WCEP) plays a crucial role in the onset and development of ENSO events (Rong et al., 2011; Chen et al., 2017). In general, this HF zonal wind activity refers to westerly wind event (WWE) and easterly wind event (EWE) with time scales less than 90 days. Due to their transient, intense, and somewhat random nature, the HF zonal wind forcing is also considered as an important factor

583 contributing to the diversity and irregularity of ENSO (Chen et al., 2015a; Fedorov et al., 2015).
 584 Motivated by this, we hypothesize that the difference in the ENSO regularity between f3-L and f3-H may
 585 arise from the differences in HF zonal wind activity.

586 To test this, we calculate the intensity of the HF zonal wind activity based on the Equations (4014)
 587 and (415). Figure 11 shows the WWI and EWI index that measures the cumulative sum of HF westerly
 588 (easterly) wind anomalies over WCEP during the ENSO development period, for the observation and the
 589 two model versions. As shown in Figure 11a, the intensity of HF westerlies in f3-H is comparable to that
 590 in the observation, with similar mean and median values. However, f3-L simulates much weaker intensity
 591 of HF westerlies. For HF easterly activity (Fig. 11b), both models show comparable statistics to the
 592 observation, with no significant differences between f3-L and f3-H. Overall, these results indicate that
 593 f3-L strongly underestimates HF westerly wind activity relative to the f3-H and the observation.



594
 595 **Figure 11.** The boxplots of the (a) WWI index and (b) EWI index during the ENSO development phase (January to
 596 August). Red, blue and black boxes indicate the f3-L, f3-H and observations, respectively. The upper and lower
 597 boundaries of the box represent the 75th and 25th percentile values, respectively. The horizontal line in the box
 598 represents the median. The black dot represents the average value.

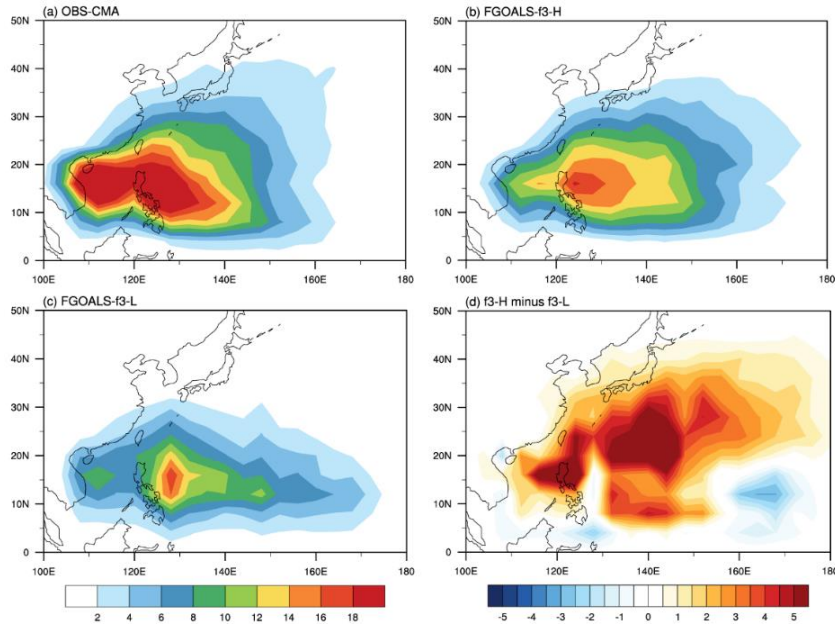
599 HF westerly wind activities are considered as semi-stochastic perturbations that modulate ENSO
 600 evolution (Gebbie et al., 2007; Gebbie and Tziperman, 2009). On the one hand, their occurrence is partly
 601 influenced by ENSO-related SSTA (Sun et al., 2020), but is also regarded as random noise independent
 602 of ENSO system (Moore and Kleeman, 1999). Most ENSO theoretical models treat HF westerly wind
 603 activity as external white noise forcing (Eisenman et al., 2005). This implies that the impact of HF activity
 604 on the coupled system depends, to some extent, on its relative magnitude relative to the ENSO amplitude.
 605 Notably, the aforementioned analysis based on the BJ index (a linear framework that excludes nonlinear

606 processes like atmospheric "noise") has shown that the coupled system simulated by f3-L is more
607 unstable than that of f3-H, hence the ENSO variability in f3-L is more prone to self-sustained oscillation.
608 Considering that the HF wind activities in f3-L is also significantly weaker than that in f3-H, from the
609 perspective of signal-to-noise ratio, this weaker "noise" is insufficient to "disrupt" the overly strong
610 ENSO oscillation in f3-L, allowing its ENSO cycle to evolve in a regular and self-sustained manner.

611 To further quantify the relative magnitude of stochastic atmospheric forcing compared to the ENSO
612 signal, we introduce an *NSR* metric, as introduced in section 2.3.5. A larger *NSR* indicates stronger
613 stochastic forcing relative to the ENSO signal. The *NSR* values are 2.67, 1.98, and 4.73 ($\text{m s}^{-1} \text{K}^{-1}$) for
614 the observation, f3-L, and f3-H, respectively. The substantially smaller *NSR* in f3-L reflects the
615 combination of its weaker HF wind activity and stronger ENSO amplitude, confirming that the stochastic
616 forcing in f3-L is insufficient to disrupt its overly intense ENSO oscillation. In contrast, the larger *NSR*
617 in f3-H indicates that stronger stochastic forcing acts on a weaker ENSO signal, facilitating the irregular
618 oscillation that more closely resembles the observation.

619 **5.2 Sources of differences in HF westerly wind activity: evaluation of TC and MJO**

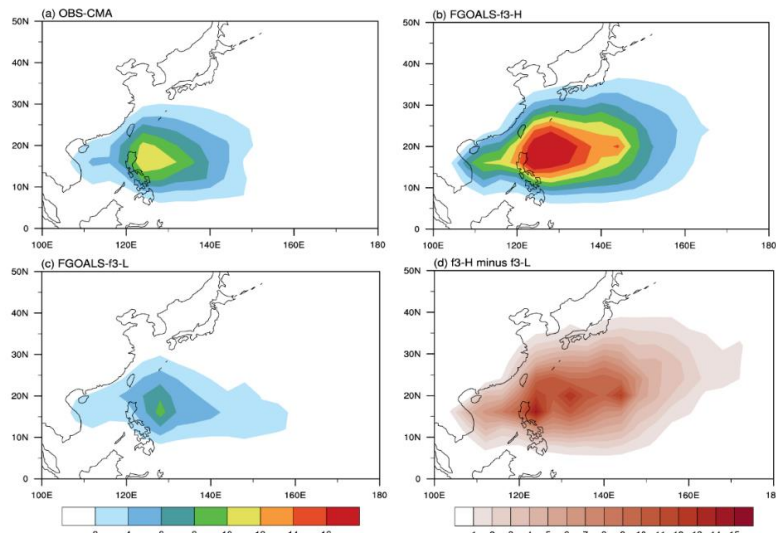
620 To further explore the origin of difference in HF westerly wind intensity between f3-L and f3-H, we
621 compare the simulated performance of TC and MJO activities in these two models. The results show that
622 the differences in the HF westerly wind intensity are primarily related to the models' ability to reproduce
623 TC activity. Figure 12 shows the spatial distribution of TCTD over the western North Pacific (WNP).
624 The spatial distributions of TCTD in both f3-H and f3-L are similar to the observation, with TC tracks
625 primarily located in the southwestern quadrant of WNP. Although both versions can reasonably
626 reproduce the spatial distribution characteristics of TC activities over the WNP, a significant difference
627 exists in TC frequency: TC activity is much more frequent in f3-H than that in f3-L. The difference map
628 (Fig. 12d, f3-H minus f3-L) shows positive values almost everywhere north of the equator. It is worth
629 noting that TCTD in f3-H remains relatively weak compared to the observation, which is a common
630 simulation bias in most current climate models (Nakamura et al., 2017; Tang et al., 2022). Although f3-
631 H still underestimates TC activity compared to the observation, this improvement relative to f3-L is
632 substantial.



633

634 **Figure 12.** The averaged TC track density (TCTD, units: counts year⁻¹) over western North Pacific for (a)
 635 Observation (CMA), (b) f3-H, (c) f3-L and (d) the difference between f3-H and f3-L (f3-H minus f3-L).

636 Furthermore, we compare the difference in the TC intensity between f3-H and f3-L. Figure 13 shows
 637 the spatial distribution of ACE index over WNP in the observation and the models. Both models show
 638 that strong TC activity is primarily concentrated east of the Philippines sea, consistent with the
 639 observation (Ma et al., 2025). However, the ACE index in f3-H is significantly stronger than that in f3-
 640 L, indicating stronger TC activity in f3-H. In summary, the TC activity over WNP is more frequent and
 641 intense in f3-H than that in f3-L, which largely explains the stronger HF westerly wind anomalies in f3-
 642 H.



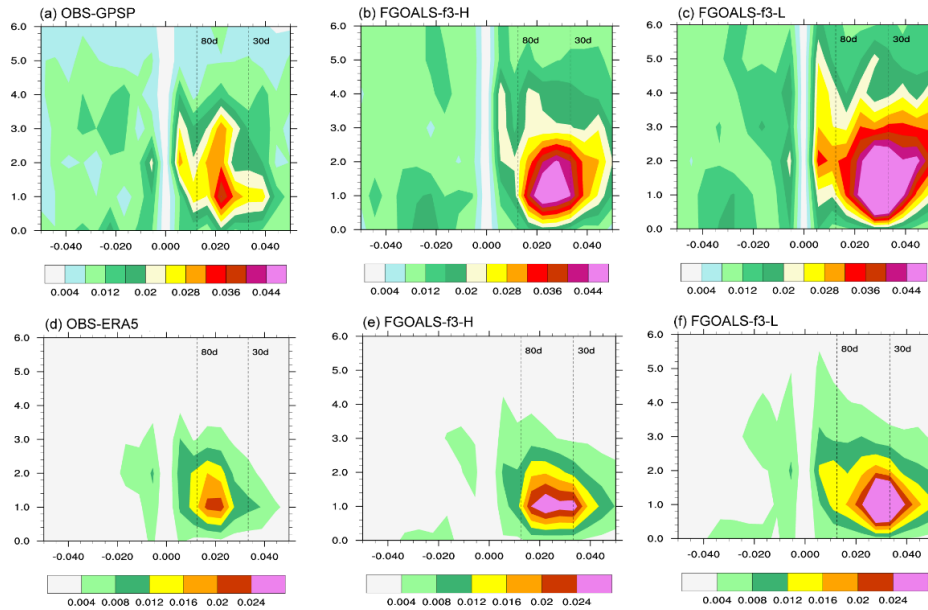
643

644 **Figure 13.** The averaged accumulated cyclone energy (ACE, units: 10⁴ knots year⁻¹) over western North Pacific for
 645 (a) Observation (CMA), (b) f3-H, (c) f3-L and (d) the difference between f3-H and f3-L (f3-H minus f3-L).

646 Model horizontal resolution is a key factor in TC simulation (Tang et al., 2022). In general, climate
647 models with coarse resolutions (≥ 100 km) tend to only reproduce TC-like structures (Camargo et al.,
648 2005; Camargo and Wing, 2016), with activity that is relatively weak and infrequent (Camargo, 2013;
649 Nakamura et al., 2017). As resolution increases, models can simulate more frequent and more intense TC
650 activity (Roberts et al., 2020a; Tang et al., 2022). In particular, when the horizontal resolution is increased
651 to 25 km, the simulation of TC spatial structure and associated wind fields is significantly improved,
652 yielding ~~a~~ more realistic characteristics of TC activity (Davis et al., 2018; Roberts et al., 2020b). The
653 analysis results of the FGOALS-f3 models (Figs. 11 and 12) are consistent with these previous findings.
654 Compared to the f3-L model (with a horizontal resolution of 100 km), the f3-H model (with a horizontal
655 resolution of 25 km) provides a more realistic simulation of TC frequency and produces stronger TC
656 intensities. This difference in TC simulation associated with model resolution modulates the intensity of
657 HF westerly wind activity and hence influences the regularity of ENSO cycle in the two models.

658 On the other hand, we also examine the other primary source of HF westerly wind activity—the MJO.
659 Figure 14 shows the wavenumber-frequency spectra of the space-time filtered precipitation and surface
660 zonal wind. It can be seen that the spectral peak of precipitation and surface zonal wind in both models
661 are concentrated at 30-80-day period, consistent with the observation. This indicates that both models
662 reproduce the observed MJO timescales reasonably well. In terms of intensity, although the MJO-related
663 precipitation and zonal wind fields are somewhat exaggerated in both models compared to the
664 observation, the difference between f3-L and f3-H is small, especially for MJO-related zonal winds.
665 Therefore, the difference in HF westerly wind activity is likely not directly linked to MJO activity.

666 Although finer resolution may improve model performance in certain aspects, these preliminary
667 results show no significant improvement in MJO simulation from 100 km to 25 km in the case of these
668 two FGOALS-f3 models. On the one hand, this may be because MJO simulation is heavily constrained
669 by the accurate representation of physical processes like convection parameterization, boundary layer
670 processes, and air-sea coupling. Thus, increased resolution must be combined with optimized physics
671 schemes to effectively improve MJO simulation (Jiang et al., 2020b). On the other hand, recent studies
672 suggest that significant MJO improvement can be seen when resolution increases to the kilometer-scale—
673 the "convection-permitting resolution" (Savarin and Chen, 2022).



674

675 **Figure 14.** Wavenumber-frequency spectra of space-time filtered (a)–(c) precipitation (units: mm/day) and (d)–(f)
 676 surface zonal wind fields (m/s) during the boreal winter (November to next August) for observation (left column),
 677 f3-H (middle column) and f3-L (right column).

678

In summary, we find that the high-resolution version can better simulate TC activity, with more
 679 frequent and stronger TCs over the WNP than the lower-resolution version. This difference results in
 680 stronger HF westerly wind activity in f3-H than that in f3-L. Given that HF westerly wind activity acts
 681 as a stochastic forcing on ENSO, the relatively weaker HF atmospheric noise in f3-L has a limited
 682 randomizing effect on its stronger ENSO signal. In other words, the weaker HF zonal wind activity in
 683 f3-L cannot overcome its inherently stronger ENSO signal, leading to overly regular oscillation in f3-L.
 684 In contrast, f3-H has a weaker intrinsic ENSO signal but stronger "noise". Therefore, the ENSO cycle in
 685 f3-L appears much more regular than that in f3-H.

686

6. Conclusions and implications

687

6.1 Conclusions

688

This study provides a process-based evaluation of how horizontal resolution influences ENSO
 689 simulation in the CAS FGOALS-f3 climate system model. The comparison between its low-resolution
 690 (f3-L, ~100 km) and high-resolution (f3-H, ~25 km) configurations reveals systematic and resolution-
 691 dependent differences in ENSO amplitude, period, oscillation ~~characteristics-irregularity~~, and underlying
 692 air-sea coupling processes.

693

A key structural source of bias in f3-L is the overly confined meridional structure of ENSO-related

694 zonal wind stress anomalies, which strengthens the thermocline and zonal-advection feedbacks and leads
695 to an exaggerated ENSO amplitude. The process-oriented diagnosis based on ENSO-related air-sea
696 coupling processes demonstrates that these feedbacks can be directly attributed to resolution-sensitive
697 meridional distribution of equatorial zonal wind stress ~~structures~~anomalies, indicating that resolving the
698 meridional structure of wind forcing is essential for realistic representation of ENSO amplitude.

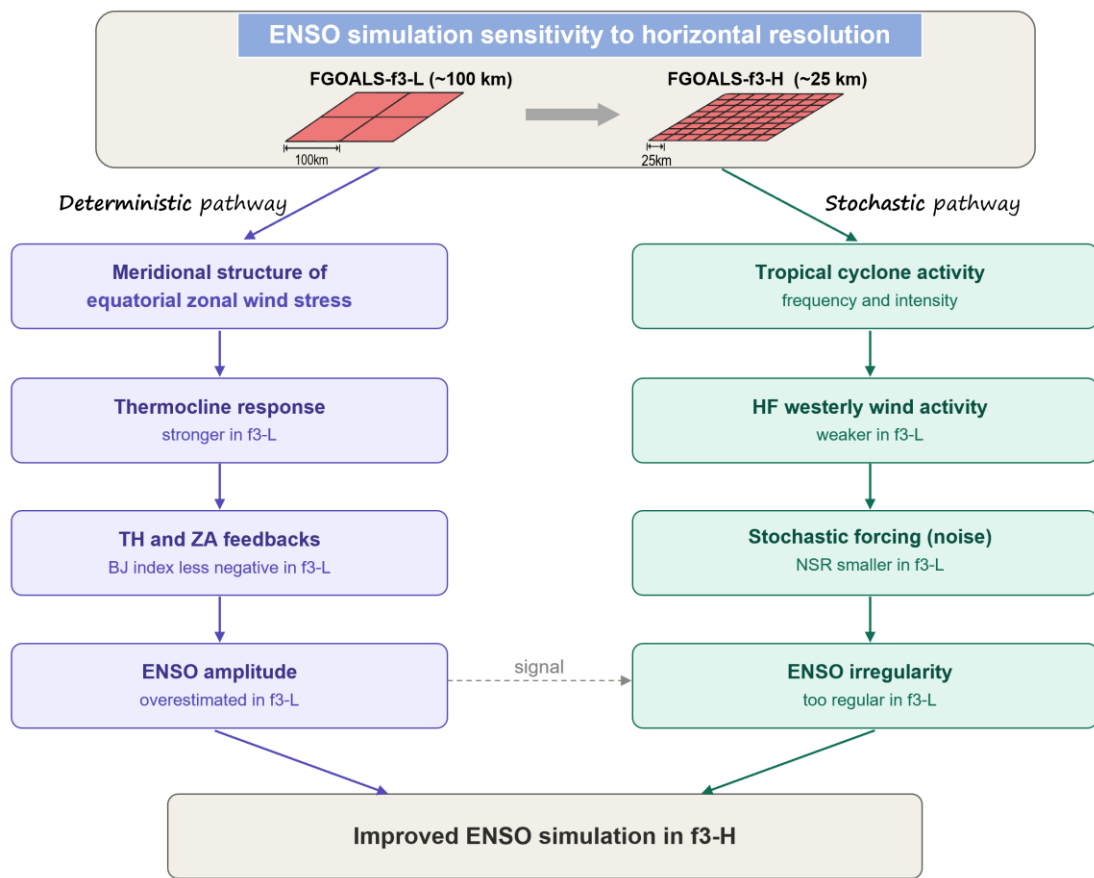
699 The excessive regularity of ENSO in f3-L is another resolution-driven bias, arising from insufficient
700 HF atmospheric variability. The high-resolution configuration produces more realistic TC activity and
701 more vigorous WWEs, which introduce stochastic forcing that disrupts the ENSO cycle and generates
702 irregular variability closer to the observation. These results highlight that the representation of synoptic-
703 scale atmospheric processes is integral to capturing ~~realistic—ENSO~~observed temporal
704 irregularity~~evolution~~ of ENSO.

705 Overall, this study demonstrates that ENSO-related biases in FGOALS-f3 arise from identifiable,
706 resolution-sensitive structural features in the coupled system. Through two complementary diagnostic
707 ~~pathways~~By quantifying feedback pathways and stochastic forcing, we provide a traceable and
708 mechanistic explanation for how horizontal resolution modulates ENSO simulation (Figure 15). The
709 ~~evaluation—diagnostic~~ framework developed here is model-agnostic and reproducible, offering a
710 practical tool for ~~diagnosing—evaluating~~ ENSO performance in other climate models and ~~can—guide~~ing
711 future development of the FGOALS-f3 model family.

712 **6.2 Implications**

713 The findings from this study yield several actionable insights for FGOALS-f3 development and for
714 the broader CMIP-class modeling community. (1) Improving the atmospheric representation of
715 equatorial wind stress meridional gradients should be a development priority. (2) As shown in Figure 15,
716 increase in R~~horizontal~~ resolution has ~~complementary~~ impacts on ~~deterministic and stochastic~~ ENSO
717 dynamics from both deterministic and stochastic pathways: the deterministic aspect influencing ENSO
718 ~~simulation—behaviors~~ is via air-sea coupling processes, and the stochastic aspect influencing ENSO
719 ~~simulation—behaviors~~ is via high-frequency HF wind activity (e.g., WWE), whose dual role both of which
720 should be explicitly considered in future model evaluation framework. (3) The diagnostics applied here
721 are model-agnostic and can serve as a reproducible framework for assessing resolution effects in other
722 climate models participating in CMIP6/CMIP7. We encourage the community to adopt the process-

723 oriented diagnostics presented here as a complement to conventional statistical metrics, so that the
 724 improvements in ENSO simulation can be traced back to specific physical mechanisms rather than
 725 assessed solely by outcome-based indices. (4) The ~25 km atmosphere resolution of f3-H improves both
 726 the air-sea coupling processes and the stochastic forcing mechanisms. ~~This supports, supporting~~ the
 727 ongoing efforts toward next-generation high-resolution climate models. However, the computational cost
 728 increases substantially from f3-L to f3-H. The low-resolution version runs on 384 processor cores and
 729 achieves a throughput of approximately 15–20 model years per wall-clock day, whereas the high-
 730 resolution version requires 6,144 processor cores and achieves only ~0.25 model years per wall-clock
 731 day. This sharp increase in computational expense makes century-scale ensemble simulations with high-
 732 resolution models, such as f3-H, considerably more demanding. Such a cost–benefit trade-off further
 733 motivates the development of variable-resolution modeling frameworks (e.g., the Model for Prediction
 734 Across Scales and the ICOSahedral Nonhydrostatic model), which can selectively refine the grid over
 735 the tropical Pacific to capture these resolution-sensitive processes while maintaining coarser resolution
 736 elsewhere.



737

738 **Figure 15.** Schematic diagram illustrating how increased horizontal resolution (~100 km to ~25 km) improves ENSO
739 simulation in FGOALS-f3 via both the deterministic feedback processes and the stochastic atmospheric forcing
740 pathways.

743
744 *Data and Code availability.* Source codes of the FGOALS-f3 model used in this study and the analysis
745 scripts are archived at [https://doi.org/https://doi.org/10.5281/zenodo.17778266](https://doi.org/10.5281/zenodo.17778266) (Song et al.,
746 [2025](https://doi.org/10.5281/zenodo.17778266)). The model output of FGOALS-f3 models described in this paper is distributed through the
747 Earth System Grid Federation (ESGF) and is freely obtained via the ESGF data portals after registration
748 (<https://aims2.llnl.gov/search>, last access: 27 November 2025). All the observation and reanalysis
749 datasets are available online and publicly available as cited in the references. The ORAS5 and ERA-5
750 datasets are obtained from <https://cds.climate.copernicus.eu/datasets>. The HadISST dataset is from
751 <https://www.metoffice.gov.uk/hadobs/hadisst/data/download.html>. The GPCP dataset is available at
752 <https://www.ncei.noaa.gov/data/global-precipitation-climatology-project-gpcp-daily/access>. The
753 SODA2.2.4 dataset can be accessed at http://apdrc.soest.hawaii.edu/datadoc/soda_2.2.4.php. The CMA
754 TC best track dataset is from <https://tcdata.typhoon.org.cn/en/zjljsjj.html>. The description and data for
755 HighResSST-present simulations of FGOALS-f3 can be found at
756 <http://doi.org/10.22033/ESGF/CMIP6.3312> (Bao and He, 2019; Bao et al., 2020).

757 *Author contribution.* All authors contributed to the study conception and design. Material preparation,
758 data collection and analysis were performed by MS and LC. JZ contributed to the application of methods
759 related to TC detection. The first draft of the manuscript was written by MS, ~~and LC and QY~~
760 ~~contributed to the writing and revising of the manuscript.~~ QY, BA and HZ discussed the results and
761 commented on the manuscript. All authors read and approved the final manuscript.

762 *Competing interests.* The authors declare that they have no conflict of interest.

763 *Disclaimer.* Publisher's note: Copernicus Publications remains neutral with regard to jurisdictional
764 claims made in the text, published maps, institutional affiliations, or any other geographical
765 representation in this paper. While Copernicus Publications makes every effort to include appropriate

766 place names, the final responsibility lies with the authors. Views expressed in the text are those of the
767 authors and do not necessarily reflect the views of the publisher.

768 *Acknowledgements.* We acknowledge the High Performance Computing Center of Nanjing University of
769 Information Science & Technology for their support of this work.

770 *Financial support.* This work was the jointly supported by the National Key Research and Development
771 Program of China (Grant 2022YFF0802004), NSFC (No. 42576024), the Excellent Youth Natural
772 Science Foundation of Jiangsu Province (BK20230061) and Postgraduate Research & Practice
773 Innovation Program of Jiangsu Province (KYCX24_1417).

774

775

776 **Reference**

777 Adler, R. F., Huffman, G. J., Chang, A., Ferraro, R., Xie, P.-P., Janowiak, J., Rudolf, B., Schneider, U.,
778 Curtis, S., Bolvin, D., Gruber, A., Susskind, J., Arkin, P., and Nelkin, E.: The version-2 global
779 precipitation climatology project (GPCP) monthly precipitation analysis (1979–present), *Journal of*
780 *Hydrometeorology*, 4, 1147–1167, [https://doi.org/10.1175/1525-](https://doi.org/10.1175/1525-7541(2003)004%3C1147:TVGPCP%3E2.0.CO;2)
781 [7541\(2003\)004%3C1147:TVGPCP%3E2.0.CO;2](https://doi.org/10.1175/1525-7541(2003)004%3C1147:TVGPCP%3E2.0.CO;2), 2003.

782 An, B., Yu, Y. Q., Bao, Q., He, B., Li, J. X., Luan, Y. H., Chen, K. J., and Zheng, W. P.: CAS FGOALS-
783 f3-H dataset for the high-resolution model intercomparison project (HighResMIP) Tier 2, *Advances*
784 *in Atmospheric Sciences*, 39, 1873–1884, <https://doi.org/10.1007/s00376-022-2030-5>, 2022.

785 Bacmeister, J. T., Wehner, M. F., Neale, R. B., Gettelman, A., Hannay, C., Lauritzen, P. H., Caron, J. M.,
786 and Truesdale, J. E.: Exploratory high-resolution climate simulations using the community
787 atmosphere model (CAM), *Journal of Climate*, 27, 3073–3099, [https://doi.org/10.1175/jcli-d-13-](https://doi.org/10.1175/jcli-d-13-00387.1)
788 [00387.1](https://doi.org/10.1175/jcli-d-13-00387.1), 2014.

789 Bao, Q., Liu, Y. M., Wu, G. X., He, B., Li, J. X., Wang, L., Wu, X. F., Chen, K. J., Wang, X. C., Yang, J.,
790 and Zhang, X. Q.: CAS FGOALS-f3-H and CAS FGOALS-f3-L outputs for the high-resolution
791 model intercomparison project simulation of CMIP6, *Atmospheric and Oceanic Science Letters*, 13,
792 576–581, <https://doi.org/10.1080/16742834.2020.1814675>, 2020.

793 Bao, Q. and He, B.: CAS FGOALS-f3-H model output prepared for CMIP6 HighResMIP highresSST-
794 present, Earth System Grid Federation [data set], <https://doi.org/10.22033/ESGF/CMIP6.3312>,
795 2019

796 Barnston, A. G., Tippett, M. K., L'Heureux, M. L., Li, S., and DeWitt, D. G.: Skill of real-time seasonal
797 ENSO model predictions during 2002–11: Is our capability increasing?, *Bulletin of the American*
798 *Meteorological Society*, 93, 631–651, <https://doi.org/10.1175/bams-d-11-00111.1>, 2012.

799 Bell, G. D., Halpert, M. S., Schnell, R. C., Higgins, R. W., Lawrimore, J., Kousky, V. E., Tinker, R.,
800 Thiaw, W., Chelliah, M., and Artusa, A.: Climate assessment for 1999, *Bulletin of the American*
801 *Meteorological Society*, 81, s1–s50, [https://doi.org/10.1175/1520-0477\(2000\)81\[s1:CAF\]2.0.CO;2](https://doi.org/10.1175/1520-0477(2000)81[s1:CAF]2.0.CO;2),
802 2000.

803 Cai, W. J., Santoso, A., Collins, M., Dewitte, B., Karamperidou, C., Kug, J.-S., Lengaigne, M., McPhaden,
804 M. J., Stuecker, M. F., Taschetto, A. S., Timmermann, A., Wu, L. X., Yeh, S.-W., Wang, G., Ng, B.,
805 Jia, F., Yang, Y., Ying, J., Zheng, X.-T., Bayr, T., Brown, J. R., Capotondi, A., Cobb, K. M., Gan, B.,
806 Geng, T., Ham, Y.-G., Jin, F.-F., Jo, H.-S., Li, X., Lin, X., McGregor, S., Park, J.-H., Stein, K., Yang,
807 K., Zhang, L., and Zhong, W. X.: Changing El Niño–Southern Oscillation in a warming climate,
808 *Nature Reviews Earth and Environment*, 2, 628–644, <https://doi.org/10.1038/s43017-021-00199-z>,
809 2021.

810 Camargo, S. J., Barnston, A. G., and Zebiak, S. E.: A statistical assessment of tropical cyclone activity in
811 atmospheric general circulation models, *Tellus A: Dynamic Meteorology and Oceanography*, 57,
812 589–604, <https://doi.org/10.3402/tellusa.v57i4.14705>, 2005.

813 Camargo, S. J.: Global and regional aspects of tropical cyclone activity in the CMIP5 models, *Journal of*
814 *Climate*, 26, 9880–9902, <https://doi.org/10.1175/jcli-d-12-00549.1>, 2013.

815 Camargo, S. J. and Wing, A. A.: Tropical cyclones in climate models, *Wiley Interdisciplinary Reviews:*
816 *Climate Change*, 7, 211–237, <https://doi.org/10.1002/wcc.373>, 2016.

817 Carton, J. A. and Giese, B. S.: A Reanalysis of Ocean Climate Using Simple Ocean Data Assimilation
818 (SODA), *Monthly Weather Review*, 136, 2999–3017, <https://doi.org/10.1175/2007mwr1978.1>,
819 2008.

820 Chang, P., Zhang, S. Q., Danabasoglu, G., Yeager, S. G., Fu, H. H., Wang, H., Castruccio, F. S., Chen,
821 Y., Edwards, J., Fu, D., Jia, Y., Laurindo, L. C., Liu, X., Rosenbloom, N., Small, R. J., Xu, G. P.,

822 Zeng, Y. H., Zhang, Q. Y., Bacmeister, J., Bailey, D. A., Duan, X., DuVivier, A. K., Li, D. P., Li, Y.
823 X., Neale, R., Stössel, A., Wang, L., Zhuang, Y., Baker, A., Bates, S., Dennis, J., Diao, X., Gan, B.
824 L., Gopal, A., Jia, D. N., Jing, Z., Ma, X., Saravanan, R., Strand, W. G., Tao, J., Yang, H. Y., Wang,
825 X. Q., Wei, Z. Q., and Wu, L. X.: An unprecedented set of high-resolution earth system simulations
826 for understanding multiscale interactions in climate variability and change, *Journal of Advances in*
827 *Modeling Earth Systems*, 12, e2020MS002298, <https://doi.org/10.1029/2020ms002298>, 2020.

828 Chen, D. K., Lian, T., Fu, C., Cane, M. A., Tang, Y. M., Murtugudde, R., Song, X. S., Wu, Q. Y., and
829 Zhou, L.: Strong influence of westerly wind bursts on El Niño diversity, *Nature Geoscience*, 8, 339–
830 345, <https://doi.org/10.1038/ngeo2399>, 2015a.

831 Chen, L., Li, T., and Yu, Y. Q.: Causes of strengthening and weakening of ENSO amplitude under global
832 warming in four CMIP5 models, *Journal of Climate*, 28, 3250–3274, [https://doi.org/10.1175/jcli-d-](https://doi.org/10.1175/jcli-d-14-00439.1)
833 [14-00439.1](https://doi.org/10.1175/jcli-d-14-00439.1), 2015b.

834 Chen, L., Yu, Y. Q., and Zheng, W. P.: Improved ENSO simulation from climate system model FGOALS-
835 g1.0 to FGOALS-g2, *Climate Dynamics*, 47, 2617–2634, [https://doi.org/10.1007/s00382-016-](https://doi.org/10.1007/s00382-016-2988-8)
836 [2988-8](https://doi.org/10.1007/s00382-016-2988-8), 2016a.

837 [Chen, L., Li, T., Behera, S. K., and Doi, T.: Distinctive precursory air–sea signals between regular and](#)
838 [super El Niños, *Advances in Atmospheric Sciences*, 33, 996–1004, \[https://doi.org/10.1007/s00376-\]\(https://doi.org/10.1007/s00376-016-5250-8\)](#)
839 [016-5250-8](#), 2016b.

840 Chen, L., Li, T., Wang, B., and Wang, L.: Formation mechanism for 2015/16 super El Nino, *Scientific*
841 *Reports*, 7, 2975–2985, <https://doi.org/10.1038/s41598-017-02926-3>, 2017.

842 Chen, L., Wang, L., Li, T., and Liu, J.: Drivers of reduced ENSO variability in mid-Holocene in a coupled
843 model, *Climate Dynamics*, 52, 5999–6014, <https://doi.org/10.1007/s00382-018-4496-5>, 2019a.

844 [Chen, L., Zheng, W., and Braconnot, P.: Towards understanding the suppressed ENSO activity during](#)
845 [mid-Holocene in PMIP2 and PMIP3 simulations, *Climate Dynamics*, 53, 1095-1110,](#)
846 [https://doi.org/10.1007/s00382-019-04637-z](#), 2019b.

847 Craig, A. P., Vertenstein, M., and Jacob, R.: A new flexible coupler for earth system modeling developed
848 for CCSM4 and CESM1, *The International Journal of High Performance Computing Applications*,
849 26, 31–42, <https://doi.org/10.1177/1094342011428141>, 2012.

850 Davis, C. A.: Resolving tropical cyclone intensity in models, *Geophysical Research Letters*, 45, 2082–

851 2087, <https://doi.org/10.1002/2017GL076966>, 2018.

852 Dawson, A., Matthews, A. J., Stevens, D. P., Roberts, M. J., and Vidale, P. L.: Importance of oceanic
853 resolution and mean state on the extra-tropical response to El Niño in a matrix of coupled models,
854 *Climate Dynamics*, 41, 1439–1452, <https://doi.org/10.1007/s00382-012-1518-6>, 2013.

855 Docquier, D., Grist, J. P., Roberts, M. J., Roberts, C. D., Semmler, T., Ponsoni, L., Massonnet, F.,
856 Sidorenko, D., Sein, D. V., Iovino, D., Bellucci, A., and Fichefet, T.: Impact of model resolution on
857 Arctic sea ice and North Atlantic Ocean heat transport, *Climate Dynamics*, 53, 4989–5017,
858 <https://doi.org/10.1007/s00382-019-04840-y>, 2019.

859 Eisenman, I., Yu, L. S., and Tziperman, E.: Westerly wind bursts: ENSO’s tail rather than the dog?,
860 *Journal of Climate*, 18, 5224–5237, <https://doi.org/10.1175/JCLI3588.1>, 2005.

861 Eyring, V., Bony, S., Meehl, G. A., Senior, C. A., Stevens, B., Stouffer, R. J., and Taylor, K. E.: Overview
862 of the Coupled Model Intercomparison Project Phase 6 (CMIP6) experimental design and
863 organization, *Geoscientific Model Development*, 9, 1937–1958, [https://doi.org/10.5194/gmd-9-](https://doi.org/10.5194/gmd-9-1937-2016)
864 1937-2016, 2016.

865 Fedorov, A. V.: The response of the coupled tropical ocean–atmosphere to westerly wind bursts,
866 *Quarterly Journal of the Royal Meteorological Society*, 128, 1–23,
867 <https://doi.org/10.1002/qj.200212857901>, 2002.

868 Fedorov, A. V., Hu, S. N., Lengaigne, M., and Guilyardi, E.: The impact of westerly wind bursts and
869 ocean initial state on the development, and diversity of El Niño events, *Climate Dynamics*, 44,
870 1381–1401, <https://doi.org/10.1007/s00382-014-2126-4>, 2015.

871 Gebbie, G., Eisenman, I., Wittenberg, A., and Tziperman, E.: Modulation of westerly wind bursts by sea
872 surface temperature: A semistochastic feedback for ENSO, *Journal of the Atmospheric Sciences*, 64,
873 3281–3295, <https://doi.org/10.1175/jas4029.1>, 2007.

874 Gebbie, G. and Tziperman, E.: Incorporating a semi-stochastic model of ocean-modulated westerly wind
875 bursts into an ENSO prediction model, *Theoretical and Applied Climatology*, 97, 65–73,
876 <https://doi.org/10.1007/s00704-008-0069-6>, 2009.

877 Griffies, S. M., Danabasoglu, G., Durack, P. J., Adcroft, A. J., Balaji, V., Böning, C. W., Chassignet, E.
878 P., Curchitser, E., Deshayes, J., Drange, H., Fox-Kemper, B., Gleckler, P. J., Gregory, J. M., Haak,
879 H., Hallberg, R. W., Heimbach, P., Hewitt, H. T., Holland, D. M., Ilyina, T., Jungclaus, J. H., Komuro,

880 Y., Krasting, J. P., Large, W. G., Marsland, S. J., Masina, S., McDougall, T. J., Nurser, A. J. G., Orr,
881 J. C., Pirani, A., Qiao, F. I., Stouffer, R. J., Taylor, K. E., Treguier, A. M., Tsujino, H., Uotila, P.,
882 Valdivieso, M., Wang, Q., Winton, M., and Yeager, S. G.: OMIP contribution to CMIP6:
883 experimental and diagnostic protocol for the physical component of the Ocean Model
884 Intercomparison Project, *Geoscientific Model Development*, 9, 3231–3296,
885 <https://doi.org/10.5194/gmd-9-3231-2016>, 2016.

886 Guilyardi, E., Gualdi, S., Slingo, J., Navarra, A., Delecluse, P., Cole, J., Madec, G., Roberts, M., Latif,
887 M., and Terray, L.: Representing El Niño in coupled ocean–atmosphere GCMs: The dominant role
888 of the atmospheric component, *Journal of Climate*, 17, 4623–4629, [https://doi.org/10.1175/JCLI-](https://doi.org/10.1175/JCLI-3260.1)
889 [3260.1](https://doi.org/10.1175/JCLI-3260.1), 2004.

890 Guilyardi, E., Capotondi, A., Lengaigne, M., Thual, S., and Wittenberg, A. T.: ENSO modeling: History,
891 progress, and challenges, in: *El Niño Southern Oscillation in a Changing Climate*, edited by:
892 McPhaden, M. J., Santoso, A., and Cai, W., American Geophysical Union, American, 199–226,
893 <https://doi.org/10.1002/9781119548164.ch9>, 2020.

894 Hallberg, R.: Using a resolution function to regulate parameterizations of oceanic mesoscale eddy effects,
895 *Ocean Modelling*, 72, 92–103, <https://doi.org/10.1016/j.ocemod.2013.08.007>, 2013.

896 Harrison, D. E. and Vecchi, G. A.: Westerly wind events in the tropical Pacific, 1986–95*, *Journal of*
897 *Climate*, 10, 3131–3156, [https://doi.org/10.1175/1520-0442\(1997\)010<3131:Wweitt>2.0.Co;2](https://doi.org/10.1175/1520-0442(1997)010<3131:Wweitt>2.0.Co;2),
898 1997.

899 He, B., Bao, Q., Wang, X. C., Zhou, L. J., Wu, X. F., Liu, Y. M., Wu, G. X., Chen, K. J., He, S. C., Hu,
900 W. T., Li, J. D., Li, J. X., Nian, G. K., Wang, L., Yang, J., Zhang, M. H., and Zhang, X. Q.: CAS
901 FGOALS-f3-L model datasets for CMIP6 historical atmospheric model intercomparison project
902 simulation, *Advances in Atmospheric Sciences*, 36, 771–778, [https://doi.org/10.1007/s00376-019-](https://doi.org/10.1007/s00376-019-9027-8)
903 [9027-8](https://doi.org/10.1007/s00376-019-9027-8), 2019.

904 He, B., He, X. Y., Liu, Y. M., Wu, G. X., Bao, Q., Hu, W. T., Sheng, C., and Feng, S. J.: Role of thermal
905 and dynamical subdaily perturbations over the Tibetan Plateau in 30-day extended-range forecast
906 of East Asian precipitation in early summer, *npj Climate and Atmospheric Science*, 8,
907 <https://doi.org/10.1038/s41612-025-00931-2>, 2025a.

908 He, X.-Y., He, B., Bao, Q., Liu, Y.-M., Li, J.-D., Wang, X.-C., Chen, X.-C., and Wu, G.-X.: The sensitivity

909 of the Asian summer monsoon simulation to horizontal resolution and air–sea coupling in the
910 FGOALS-f climate system model, *Advances in Climate Change Research*, 16, 44 – 57,
911 <https://doi.org/10.1016/j.accre.2025.01.008>, 2025b.

912 Hersbach, H., Bell, B., Berrisford, P., Hirahara, S., Horányi, A., Muñoz-Sabater, J., Nicolas, J., Peubey,
913 C., Radu, R., Schepers, D., Simmons, A., Soci, C., Abdalla, S., Abellan, X., Balsamo, G., Bechtold,
914 P., Biavati, G., Bidlot, J., Bonavita, M., De Chiara, G., Dahlgren, P., Dee, D., Diamantakis, M.,
915 Dragani, R., Flemming, J., Forbes, R., Fuentes, M., Geer, A., Haimberger, L., Healy, S., Hogan, R.
916 J., Hólm, E., Janisková, M., Keeley, S., Laloyaux, P., Lopez, P., Lupu, C., Radnoti, G., de Rosnay,
917 P., Rozum, I., Vamborg, F., Villaume, S., and Thépaut, J. N.: The ERA5 global reanalysis, *Quarterly*
918 *Journal of the Royal Meteorological Society*, 146, 1999–2049, <https://doi.org/10.1002/qj.3803>,
919 2020.

920 Hewitt, H. T., Roberts, M. J., Hyder, P., Graham, T., Rae, J., Belcher, S. E., Bourdallé-Badie, R., Copsey,
921 D., Coward, A., Guiavarch, C., Harris, C., Hill, R., Hirschi, J. J. M., Madec, G., Mizielinski, M. S.,
922 Neininger, E., New, A. L., Rioual, J.-C., Sinha, B., Storkey, D., Shelly, A., Thorpe, L., and Wood,
923 R. A.: The impact of resolving the Rossby radius at mid-latitudes in the ocean: results from a high-
924 resolution version of the Met Office GC2 coupled model, *Geoscientific Model Development*, 9,
925 3655–3670, <https://doi.org/10.5194/gmd-9-3655-2016>, 2016.

926 Hua, L. J., Chen, L., Rong, X. Y., Su, J. Z., Wang, L., Li, T., and Yu, Y. Q.: Impact of atmospheric model
927 resolution on simulation of ENSO feedback processes: a coupled model study, *Climate Dynamics*,
928 51, 3077–3092, <https://doi.org/10.1007/s00382-017-4066-2>, 2018.

929 Hunke, E. C. and Lipscomb, W. H.: CICE: The Los Alamos Sea Ice Model, *Documentation and Software*
930 *User’s Manual, Version 4.1*, Tech. Rep. LA-CC-06-012, Los Alamos National Laboratory, Los
931 Alamos, New Mexico, available at: <http://oceans11.lanl.gov/trac/CICE>, 2010.

932 Jiang, W. P., Huang, P., Li, G., and Huang, G.: Emergent constraint on the frequency of central Pacific
933 El Niño under global warming by the equatorial Pacific cold tongue bias in CMIP5/6 models,
934 *Geophysical Research Letters*, 47, <https://doi.org/10.1029/2020gl089519>, 2020a.

935 Jiang, W. P., Huang, P., Huang, G., and Ying, J.: Origins of the excessive westward extension of ENSO
936 SST simulated in CMIP5 and CMIP6 models, *Journal of Climate*, 34, 2839–2851,
937 <https://doi.org/10.1175/jcli-d-20-0551.1>, 2021.

938 Jiang, X. N., Adames, Á. F., Kim, D., Maloney, E. D., Lin, H., Kim, H., Zhang, C. D., DeMott, C. A.,
939 and Klingaman, N. P.: Fifty years of research on the Madden-Julian Oscillation: Recent progress,
940 challenges, and perspectives, *Journal of Geophysical Research: Atmospheres*, 125,
941 <https://doi.org/10.1029/2019jd030911>, 2020b.

942 Jin, F.-F.: An equatorial ocean recharge paradigm for ENSO. Part I: Conceptual model, *Journal of the*
943 *Atmospheric Sciences*, 54, 811–829, [https://doi.org/10.1175/1520-](https://doi.org/10.1175/1520-0469(1997)054<0811:Aeorpf>2.0.Co;2)
944 [0469\(1997\)054<0811:Aeorpf>2.0.Co;2](https://doi.org/10.1175/1520-0469(1997)054<0811:Aeorpf>2.0.Co;2), 1997.

945 Jin, F. F., Kim, S. T., and Bejarano, L.: A coupled-stability index for ENSO, *Geophysical Research Letters*,
946 33, <https://doi.org/10.1029/2006gl027221>, 2006.

947 Kim, S. T. and Jin, F.-F.: An ENSO stability analysis. Part II: Results from the twentieth and twenty-first
948 century simulations of the CMIP3 models, *Climate Dynamics*, 36, 1609–1627,
949 <https://doi.org/10.1007/s00382-010-0872-5>, 2011a.

950 Kim, S. T. and Jin, F.-F.: An ENSO stability analysis. Part I: results from a hybrid coupled model, *Climate*
951 *Dynamics*, 36, 1593–1607, <https://doi.org/10.1007/s00382-010-0796-0>, 2011b.

952 Kreussler, P., Caron, L. P., Wild, S., Loosveldt Tomas, S., Chauvin, F., Moine, M. P., Roberts, M. J.,
953 Ruprich-Robert, Y., Seddon, J., Valcke, S., Vannière, B., and Vidale, P. L.: Tropical cyclone
954 integrated kinetic energy in an ensemble of HighResMIP simulations, *Geophysical Research Letters*,
955 48, <https://doi.org/10.1029/2020gl090963>, 2021.

956 Lawrence, D. M., Oleson, K. W., Flanner, M. G., Thornton, P. E., Swenson, S. C., Lawrence, P. J., Zeng,
957 X., Yang, Z. L., Levis, S., and Sakaguchi, K.: Parameterization improvements and functional and
958 structural advances in version 4 of the Community Land Model, *Journal of Advances in Modeling*
959 *Earth Systems*, 3, <https://doi.org/10.1029/2011MS00045>, 2011.

960 Li, J., Yu, Y. Q., and Sun, D. Z.: Asymmetric Responses in the Equatorial Pacific to Wind Forcing in
961 OMIP2 Experiments: Role of Zonal Currents, *Geophysical Research Letters*, 52, e2025GL114661,
962 <https://doi.org/10.1029/2025gl114661>, 2025.

963 Li, J. X., Bao, Q., Liu, Y. M., Wang, L., Yang, J., Wu, G. X., Wu, X. F., He, B., Wang, X. C., Zhang, X.
964 Q., Yang, Y. X., and Shen, Z. L.: Effect of horizontal resolution on the simulation of tropical
965 cyclones in the Chinese Academy of Sciences FGOALS-f3 climate system model, *Geoscientific*
966 *Model Development*, 14, 6113–6133, <https://doi.org/10.5194/gmd-14-6113-2021>, 2021.

967 Li, T.: Phase transition of the El Niño–Southern Oscillation: A stationary SST mode, *Journal of the*
968 *atmospheric sciences*, 54, 2872–2887, [https://doi.org/10.1175/1520-](https://doi.org/10.1175/1520-0469(1997)054<2872:PTOTEN>2.0.CO;2)
969 [0469\(1997\)054<2872:PTOTEN>2.0.CO;2](https://doi.org/10.1175/1520-0469(1997)054<2872:PTOTEN>2.0.CO;2), 1997.

970 Li, T. Y., Yu, Y. Q., An, B., Luan, Y. H., and Chen, K. J.: Tropical instability waves in a high-resolution
971 oceanic and coupled GCM, *Ocean Modelling*, 182, <https://doi.org/10.1016/j.ocemod.2023.102169>,
972 2023.

973 Li, Y., Liu, H., Ding, M., Lin, P., Yu, Z., Yu, Y., Meng, Y., Li, Y., Jian, X., and Jiang, J.: Eddy-resolving
974 simulation of CAS-LICOM3 for phase 2 of the ocean model intercomparison project, *Advances in*
975 *Atmospheric Sciences*, 37, 1067–1080, <https://doi.org/10.1007/s00376-020-0057-z>, 2020.

976 Liang, Y. and Fedorov, A. V.: Linking the Madden–Julian Oscillation, tropical cyclones and westerly
977 wind bursts as part of El Niño development, *Climate Dynamics*, 57, 1039–1060,
978 <https://doi.org/10.1007/s00382-021-05757-1>, 2021.

979 Liao, H. X., Cai, Z. C., Guo, J. S., and Song, Z. Y.: Effects of ITCZ poleward location bias on ENSO
980 seasonal phase-locking simulation in climate models, *Journal of Climate*, 36, 5233–5249,
981 <https://doi.org/10.1175/jcli-d-22-0891.1>, 2023.

982 Lu, B., Jin, F.-F., and Ren, H.-L.: A coupled dynamic index for ENSO periodicity, *Journal of Climate*,
983 31, 2361–2376, <https://doi.org/10.1175/jcli-d-17-0466.1>, 2018.

984 Lu, X. Q., Yu, H., Ying, M., Zhao, B. K., Zhang, S., Lin, L. M., Bai, L. N., and Wan, R. J.: Western north
985 Pacific tropical cyclone database created by the China Meteorological Administration, *Advances in*
986 *Atmospheric Sciences*, 38, 690–699, <https://doi.org/https://10.1007/s00376-020-0211-7>, 2021.

987 Ma, T., Yu, W.-D., Speich, S., Zhao, H.-K., Xin, R., Luo, H., and Wu, L.-G.: Philippine archipelago and
988 South China Sea monsoon plus ocean cooling buffer Northwestern Pacific super typhoons, *Nature*
989 *Communications*, 16, <https://doi.org/10.1038/s41467-025-62334-4>, 2025.

990 Madden, R. A. and Julian, P. R.: Detection of a 40–50 day oscillation in the zonal wind in the tropical
991 Pacific, *Journal of Atmospheric Sciences*, 28, 702–708, [https://doi.org/10.1175/1520-](https://doi.org/10.1175/1520-0469(1971)028%3C0702:DOADOI%3E2.0.CO;2)
992 [0469\(1971\)028%3C0702:DOADOI%3E2.0.CO;2](https://doi.org/10.1175/1520-0469(1971)028%3C0702:DOADOI%3E2.0.CO;2), 1971.

993 Madden, R. A. and Julian, P. R.: Description of global-scale circulation cells in the tropics with a 40–50
994 day period, *Journal of Atmospheric Sciences*, 29, 1109–1123, [https://doi.org/10.1175/1520-](https://doi.org/10.1175/1520-0469(1972)029%3C1109:DOGSCC%3E2.0.CO;2)
995 [0469\(1972\)029%3C1109:DOGSCC%3E2.0.CO;2](https://doi.org/10.1175/1520-0469(1972)029%3C1109:DOGSCC%3E2.0.CO;2), 1972.

996 McPhaden, M. J., Zebiak, S. E., and Glantz, M. H.: ENSO as an integrating concept in earth science,
997 *Science*, 314, 1740–1745, <https://doi.org/10.1126/science.1132588>, 2006.

998 Moore, A. M. and Kleeman, R.: Stochastic forcing of ENSO by the intraseasonal oscillation, *Journal of*
999 *Climate*, 12, 1199–1220, [https://doi.org/10.1175/1520-0442\(1999\)012<1199:Sfoebt>2.0.Co;2](https://doi.org/10.1175/1520-0442(1999)012<1199:Sfoebt>2.0.Co;2),
1000 1999.

1001 Nakamura, J., Camargo, S. J., Sobel, A. H., Henderson, N., Emanuel, K. A., Kumar, A., LaRow, T. E.,
1002 Murakami, H., Roberts, M. J., Scoccimarro, E., Vidale, P. L., Wang, H., Wehner, M. F., and Zhao,
1003 M.: Western North Pacific Tropical Cyclone Model Tracks in Present and Future Climates, *Journal*
1004 *of Geophysical Research: Atmospheres*, 122, 9721–9744, <https://doi.org/10.1002/2017jd027007>,
1005 2017.

1006 Navarra, A., Gualdi, S., Masina, S., Behera, S., Luo, J. J., Masson, S., Guilyardi, E., Delecluse, P., and
1007 Yamagata, T.: Atmospheric horizontal resolution affects tropical climate variability in coupled
1008 models, *Journal of Climate*, 21, 730–750, <https://doi.org/10.1175/2007jcli1406.1>, 2008.

1009 Planton, Y. Y., Guilyardi, E., Wittenberg, A. T., Lee, J., Gleckler, P. J., Bayr, T., McGregor, S., McPhaden,
1010 M. J., Power, S., Roehrig, R., Vialard, J., and Voltaire, A.: Evaluating climate models with the
1011 CLIVAR 2020 ENSO metrics package, *Bulletin of the American Meteorological Society*, 102,
1012 E193–E217, <https://doi.org/10.1175/bams-d-19-0337.1>, 2021.

1013 Rayner, N. A., Parker, D. E., Horton, E. B., Folland, C. K., Alexander, L. V., Rowell, D. P., Kent, E. C.,
1014 and Kaplan, A.: Global analyses of sea surface temperature, sea ice, and night marine air
1015 temperature since the late nineteenth century, *Journal of Geophysical Research: Atmospheres*, 108,
1016 <https://doi.org/10.1029/2002jd002670>, 2003.

1017 Roberts, M. J., Camp, J., Seddon, J., Vidale, P. L., Hodges, K., Vanniere, B., Mecking, J., Haarsma, R.,
1018 Bellucci, A., Scoccimarro, E., Caron, L.-P., Chauvin, F., Terray, L., Valcke, S., Moine, M.-P.,
1019 Putrasahan, D., Roberts, C., Senan, R., Zarzycki, C., and Ullrich, P.: Impact of model resolution on
1020 tropical cyclone simulation using the HighResMIP–PRIMAVERA multimodel ensemble, *Journal*
1021 *of Climate*, 33, 2557–2583, <https://doi.org/10.1175/jcli-d-19-0639.1>, 2020a.

1022 Roberts, M. J., Camp, J., Seddon, J., Vidale, P. L., Hodges, K., Vannière, B., Mecking, J., Haarsma, R.,
1023 Bellucci, A., Scoccimarro, E., Caron, L. P., Chauvin, F., Terray, L., Valcke, S., Moine, M. P.,
1024 Putrasahan, D., Roberts, C. D., Senan, R., Zarzycki, C., Ullrich, P., Yamada, Y., Mizuta, R., Kodama,

1025 C., Fu, D., Zhang, Q., Danabasoglu, G., Rosenbloom, N., Wang, H., and Wu, L.: Projected future
1026 changes in tropical cyclones using the CMIP6 HighResMIP multimodel ensemble, *Geophysical*
1027 *Research Letters*, 47, e2020GL088662, <https://doi.org/10.1029/2020gl088662>, 2020b.

1028 Roberts, M. J., Reed, K. A., Bao, Q., Barsugli, J. J., Camargo, S. J., Caron, L.-P., Chang, P., Chen, C.-T.,
1029 Christensen, H. M., Danabasoglu, G., Frenger, I., Fučkar, N. S., ul Hasson, S., Hewitt, H. T., Huang,
1030 H., Kim, D., Kodama, C., Lai, M., Leung, L.-Y. R., Mizuta, R., Nobre, P., Ortega, P., Paquin, D.,
1031 Roberts, C. D., Scoccimarro, E., Seddon, J., Treguier, A. M., Tu, C.-Y., Ullrich, P. A., Vidale, P. L.,
1032 Wehner, M. F., Zarzycki, C. M., Zhang, B., Zhang, W., and Zhao, M.: High-Resolution model
1033 intercomparison project phase 2 (HighResMIP2) towards CMIP7, *Geoscientific Model*
1034 *Development*, 18, 1307–1332, <https://doi.org/10.5194/gmd-18-1307-2025>, 2025.

1035 Rong, X. Y., Zhang, R. H., Li, T., and Su, J. Z.: Upscale feedback of high-frequency winds to ENSO,
1036 *Quarterly Journal of the Royal Meteorological Society*, 137, 894–907,
1037 <https://doi.org/10.1002/qj.804>, 2011.

1038 Savarin, A. and Chen, S. S.: Pathways to better prediction of the MJO:1. Effects of model resolution and
1039 moist physics on Atmospheric boundary layer and precipitation, *Journal of Advances in Modeling*
1040 *Earth Systems*, 14, e2021MS002928, <https://doi.org/10.1029/2021ms002929>, 2022.

1041 Small, R. J., Bryan, F. O., Bishop, S. P., and Tomas, R. A.: Air–Sea turbulent heat fluxes in climate models
1042 and observational analyses: What drives their variability?, *Journal of Climate*, 32, 2397–2421,
1043 <https://doi.org/10.1175/jcli-d-18-0576.1>, 2019.

1044 Song, M.: The code of FGOALS-f3 model study, Zenodo [code],
1045 <https://doi.org/10.5281/zenodo.17778266>, 2025.

1046 Su, J. Z., Zhang, R. H., Li, T., Rong, X. Y., Kug, J. S., and Hong, C.-C.: Causes of the El Niño and La
1047 Niña amplitude asymmetry in the equatorial eastern Pacific, *Journal of Climate*, 23, 605–617,
1048 <https://doi.org/10.1175/2009jcli2894.1>, 2010.

1049 Su, J. Z., Li, T., and Zhang, R. H.: The initiation and developing mechanisms of central Pacific El Niños,
1050 *Journal of Climate*, 27, 4473–4485, <https://doi.org/10.1175/jcli-d-13-00640.1>, 2014.

1051 Sun, M., Li, T., and Chen, L.: El Niño phase-dependent high-frequency variability in western equatorial
1052 Pacific, *Climate Dynamics*, 55, 2165–2184, <https://doi.org/10.1007/s00382-020-05376-2>, 2020.

1053 Tang, Y. L., HuangFu, J. I., Huang, R. H., and Chen, W.: Simulation and projection of tropical cyclone

1054 activities over the western North Pacific by CMIP6 HighResMIP, *Climate Dynamics*, 35, 7771–
1055 7794, <https://doi.org/10.1175/JCLI-D-21-0760.1>, 2022.

1056 Thomson, D. J.: Spectrum estimation and harmonic analysis, *Proceedings of the IEEE*, 79, 1055-1096,
1057 <https://doi.org/10.1109/PROC.1982.12433>, 1982.

1058 Timmermann, A., An, S. I., Kug, J. S., Jin, F. F., Cai, W., Capotondi, A., Cobb, K. M., Lengaigne, M.,
1059 McPhaden, M. J., Stuecker, M. F., Stein, K., Wittenberg, A. T., Yun, K. S., Bayr, T., Chen, H. C.,
1060 Chikamoto, Y., Dewitte, B., Dommenges, D., Grothe, P., Guilyardi, E., Ham, Y. G., Hayashi, M.,
1061 Ineson, S., Kang, D., Kim, S., Kim, W., Lee, J. Y., Li, T., Luo, J. J., McGregor, S., Planton, Y., Power,
1062 S., Rashid, H., Ren, H. L., Santoso, A., Takahashi, K., Todd, A., Wang, G., Wang, G., Xie, R., Yang,
1063 W. H., Yeh, S. W., Yoon, J., Zeller, E., and Zhang, X.: El Niño-Southern Oscillation complexity,
1064 *Nature*, 559, 535–545, <https://doi.org/10.1038/s41586-018-0252-6>, 2018.

1065 [Wang, L., Li, T., and Zhou, T. J.: Intraseasonal SST variability and air-sea interaction over the Kuroshio](https://doi.org/10.1175/JCLI-D-11-00109.1)
1066 [extension region during boreal summer. *Journal of Climate*, 25, 1619–1634,](https://doi.org/10.1175/JCLI-D-11-00109.1)
1067 <https://doi.org/10.1175/JCLI-D-11-00109.1>, 2012.

1068 [Wei, X. J. Chen, L., and Sun, M.: Fine-tuning Atmospheric Parameters for Improving ENSO Simulation](https://doi.org/10.1007/s00376-025-4423-8)
1069 [in the Zebiak–Cane Model. *Advances in Atmospheric Science*, 43, 420–435,](https://doi.org/10.1007/s00376-025-4423-8)
1070 <https://doi.org/10.1007/s00376-025-4423-8>, 2026.

1071 Yan, Y. and Sun, D.-Z.: Phase-Locking of El Niño and La Niña events in CMIP6 models, *Atmosphere*,
1072 15, 882, <https://doi.org/10.3390/atmos15080882>, 2024.

1073 Ying, J., Lian, T., Ren, H.-L., Zhang, C., Liu, T., and Tan, X.-X.: Effects of tropical cyclones on ENSO,
1074 *Journal of Climate*, 32, 6423–6443, <https://doi.org/10.1175/jcli-d-18-0821.1>, 2019.

1075 Ying, M., Zhang, W., Yu, H., Lu, X. Q., Feng, J. X., Fan, Y. X., Zhu, Y. t., and Chen, D. Q.: An overview
1076 of the China Meteorological Administration tropical cyclone database, *Journal of Atmospheric and*
1077 *Oceanic Technology*, 31, 287–301, [https://doi.org/https://10.1175/JTECH-D-12-00119.1](https://doi.org/10.1175/JTECH-D-12-00119.1), 2014.

1078 Yu, Y. Q., An, B., Liu, H. L., Bao, Q., Lin, P. F., He, B., Zheng, W. P., Luan, Y. H., Bai, R. and Li, T. Y.:
1079 Review of the development and application of the high-resolution climate system model FGOALS,
1080 *Chinese Journal of Atmospheric Sciences (in Chinese)*, 48, 200-217,
1081 <https://doi.org/10.1007/BF02915571>, 2024.

1082 Yu, Y. Q., Tang, S. L., Liu, H. L., Lin, P. F., and Li, X. L.: Development and evaluation of the dynamic

1083 framework of an ocean general circulation model with arbitrary orthogonal curvilinear coordinate,
1084 Chinese Journal of Atmospheric Sciences (in Chinese), 42, 877–889,
1085 <https://doi.org/10.3878/j.issn.1006-9895.1805.17284>, 2018.

1086 Zhang, R.-H., Yu, Y. Q., Song, Z. Y., Ren, H.-L., Tang, Y. M., Qiao, F. I., Wu, T. W., Gao, C., Hu, J. Y.,
1087 Tian, F., Zhu, Y. C., Chen, L., Liu, H. L., Lin, P. F., Wu, F. H., and Wang, L.: A review of progress
1088 in coupled ocean-atmosphere model developments for ENSO studies in China, Journal of
1089 Oceanology and Limnology, 38, 930–961, <https://doi.org/10.1007/s00343-020-0157-8>, 2020.

1090 Zhao, J. W., Wang, F., Zhan, R. F., Guo, Y. P., Huang, X., and Liu, C.: How Does Tropical Cyclone
1091 Genesis Frequency Respond to a Changing Climate?, Geophysical Research Letters, 50,
1092 <https://doi.org/10.1029/2023gl102879>, 2023.

1093 Zhao, Y. D. and Sun, D.-Z.: ENSO asymmetry in CMIP6 models, Journal of Climate, 35, 5555–5572,
1094 <https://doi.org/10.1175/jcli-d-21-0835.1>, 2022.

1095 Zhou, L., Bao, Q., Liu, Y. M., Wu, G. X., Wang, W. C., Wang, X. C., He, B., Yu, H. Y., and Li, J. D.:
1096 Global energy and water balance: Characteristics from Finite-volume Atmospheric Model of the
1097 IAP/LASG (FAMIL 1), Journal of Advances in Modeling Earth Systems, 7, 1–20,
1098 <https://doi.org/10.1002/2014MS000349>, 2015.

1099 Zi, P., Liu, Y. M., Li, J. D., Yang, R. W., He, B., and Bao, Q.: Reduced Spring Precipitation Bias and
1100 Associated Physical Causes over South China in FGOALS-f3 Climate Models: Experiments with
1101 the Horizontal Resolutions, Journal of Meteorological Research, 38, 784–804,
1102 <https://doi.org/10.1007/s13351-024-3200-4>, 2024.

1103 Zuo, H., Balmaseda, M. A., Tietsche, S., Mogensen, K., and Mayer, M.: The ECMWF operational
1104 ensemble reanalysis–analysis system for ocean and sea ice: A description of the system and
1105 assessment, Ocean Science, 15, 779–808, <https://doi.org/10.5194/os-15-779-2019>, 2019.